*Permafrost and Periglacial Processes*

WILEY

RESEARCH ARTICLE OPEN ACCESS

# A Decade of Post-Fire Succession Amplifies the Effect of Wildfire on the Surface Radiation Balance and Permafrost Thaw in Subarctic Peatlands

Maude Auclair[1] | Stephanie N. Wright[2] | David Olefeldt[3] | Oliver Sonnentag[4] | William L. Quinton[1]

[1]Cold Regions Research Centre, Wilfrid Laurier University, Waterloo, Ontario, Canada | [2]Department of Civil Engineering, Queen's University, Kingston, Ontario, Canada | [3]Department of Renewable Resources, University of Alberta, Edmonton, Alberta, Canada | [4]Département de Géographie, Université de Montréal, Montréal, Québec, Canada

**Correspondence:** Stephanie N. Wright (stephanie.wright@queensu.ca)

**Received:** 15 July 2025 | **Revised:** 19 October 2025 | **Accepted:** 28 October 2025

**Funding:** We gratefully acknowledge Łíídlı̨ı̨ Kų́ę́ First Nation, on whose traditional lands this research was conducted. This research was funded by ArcticNet. DO received support for the research from the National Science and Engineering Research Council Discovery grant (RGPIN-2016-04688). OS acknowledges support through the Canada Research Chair (CRC-2018-279 00259), NSERC Discovery Grants (DGPIN-280 2018-05743) and FQRNT Projet de Recherche en Équipe programs (RQ000082), and the Global Water Futures project.

**Keywords:** climate change | peatlands | permafrost thaw | radiation balance | talik | wildfire

## ABSTRACT

Increasing wildfire activity is driving permafrost thaw in subarctic peatlands across the southern Northwest Territories, but the key mechanisms and progression of thaw following fire remain poorly understood. In response, 10 years (2015–2024) of near-continuous surface (four-component radiation, wind, and snow) and subsurface measurements (temperature, moisture, and frost tables) were examined from a burned and unburned permafrost peatland in the southern Taiga Plains ecoregion. A low-severity wildfire in 2014 burned a portion of a peat plateau with stunted black spruce, which led to full tree mortality but left most dead trees standing. Results indicated that wildfire increased the rate of permafrost thaw (4 cm year$^{-1}$ higher on average), smoothed the permafrost table topography, and led to 100% talik extent (perennially unfrozen layer above permafrost) within 8 years following the fire. Post-fire succession during the first decade, including the gradual toppling of dead burnt trees, ultimately amplified the energy available for ground heating and permafrost thaw. In contrast, the immediate reduction in albedo and snowpack alterations following fire had either only short-term effects or even cooling effects. This study demonstrated that summertime processes outweighed wintertime processes in driving permafrost thaw, suggesting the effects of wildfire may intensify in the future as winters shorten under current climate warming projections. Considering millions of hectares in the Northwest Territories have recently burned, findings from this study directly support projections of permafrost thaw and resulting land cover changes driven by regional wildfire disturbance coupled with ongoing climate warming.

## 1 | Introduction

The northern boreal region in Canada's Northwest Territories (NWT) is warming at rates unprecedented in the climate record [1], leading to rapid and widespread permafrost thaw [2]. Thaw is transforming land cover types [3] and intensifying geomorphic (e.g., [4]), hydrological (e.g., [5, 6]), and biogeochemical cycles (e.g., [7]), as well as surface-atmosphere interactions (e.g., [8]). The gradual effects of climate change on permafrost are intensified by those of pulse disturbances such as wildfires [9]. Discontinuous permafrost in this region can be generally classified as "climate-driven, ecosystem protected" [10, 11],

where permafrost that once formed under colder climates now persists due to ecosystem protections such as soil type and saturation (e.g., peat and fine-grained soils). Disturbances like wildfire can damage ecosystem protections, resulting in permafrost thaw that will not recover to pre-fire conditions, although it may take decades to centuries for complete permafrost loss [10, 12]. Despite the large body of literature demonstrating that wildfire leads to permafrost thaw (e.g., [9, 12–14]), there remains a gap in understanding the mechanisms driving thaw (e.g., canopy loss, summer albedo, soil thermal conductivity, and snow dynamics), which limits the ability to predict associated changes to ecosystems, biogeochemical cycling, and hydrology. The importance of understanding how wildfire affects sensitive permafrost systems will likely continue to increase given that wildfire occurrence is projected to increase in frequency, severity, and magnitude in the northern hemisphere in the coming decades [15–19].

Mean annual air temperature and therefore permafrost temperature have steadily risen throughout the Taiga Plains ecoregion since the mid-1970s [11, 20–22]. In the southern Taiga Plains, permafrost is preferentially located in boreal peatland complexes below forested peat plateaus [23–26], where it is ecosystem-protected by a relatively thick and thermally insulative unsaturated peat layer during the short summer [27–29]. Wildfire disproportionately affects peat plateaus relative to treeless bogs and fens, since they contain more fuel in tree canopies, have relatively dry ground surfaces, and thicker unsaturated layers [21, 30]. Immediately following wildfire, the ground warms (within days to months) and the active layer thickness (ALT) gradually increases [14]. If the maximum annual thaw depth increases beyond a site-specific threshold (e.g., 0.6–0.8 m at Scotty Creek, NWT; [31]), the active layer can no longer completely refreeze in winter and a suprapermafrost talik forms [32], which is a "tipping point" that can accelerate the rate of thaw fivefold [33]. Over the last 30 years in the southern Taiga Plains, wildfire was directly responsible for increased talik extent from 20% in unburned sites to 70%–100% in burned sites and led to ~25% of all thermokarst wetland expansion in the region [12]. Talik formation in peat plateaus results in accelerated thaw-induced subsidence, surface inundation, and a transition from tree-covered plateaus to treeless and permafrost-free thermokarst wetlands or lakes [12, 34, 35]. Although other studies (e.g., [12, 36]) have demonstrated the link between wildfire and talik occurrence, they leave gaps in understanding the timing of talik development along with the key responsible mechanisms and thresholds for talik formation.

Wildfire typically results in warmer ground temperatures by directly altering the surface energy balance through several summertime and wintertime processes, but the relative importance of these processes is poorly understood [9]. For example, wildfire may increase ground temperatures in summer by increasing incoming solar radiation through the removal of the tree canopy [37, 38] and decreasing surface albedo through charring the ground surface [39]. Both changes can lead to more uniform surface energy inputs that dampen variations in the underlying frost table topography and alter soil drainage patterns through talik formation [40]. Yet, burnt peat can create a hydrophobic layer that reduces infiltration and soil moisture [41], possibly promoting drier and more insulative soils that would serve as protection for underlying permafrost. In contrast, reduced evapotranspiration resulting from the loss of vascular vegetation can increase near-surface soil moisture content and therefore enhance ground cooling in the winter in the absence of snowpack changes [9]. The onset and progression of these changes have not been well documented and will vary depending on burn severity and permafrost landform, among others.

In winter, a reduced tree canopy from fire alters snowpack dynamics. The loss of tree canopy negates canopy interception of snow, particularly in dense forests, resulting in greater accumulation on the ground, but it also results in greater exposure of the snowpack to erosion and compaction by wind, and higher ablation rates in spring [14, 16, 40]. Deeper snowpacks following wildfire can thermally insulate the ground during winter [42], but this can be counteracted by a more rapid late winter snowmelt driven by increased direct solar radiation and by a lower albedo resulting from ash-covered snowpack surfaces [43, 44]. Ground warming from wildfire may also be offset by canopy reduction or removal enabling greater radiative cooling due to reduced longwave downwelling from a diminished tree canopy [45], and greater ventilation due to increased wind turbulence over the snowpack surface [46, 47]. Representing these complex processes in process-based models remains challenging, and limited empirical data have led, in part, to a disconnect between field results and model predictions for boreal peatland resiliency to wildfire [9].

The competing and compounding effects of wildfire on ground surface and subsurface energy and water flow and storage processes remain poorly understood. Wintertime and summertime processes may be working together or in opposition to alter coupled water and heat transfer, yet most studies focusing on these processes are generally short-term (1–2 years) and occur either immediately/closely after a fire (e.g., [40]) or after several years (e.g., [36]). Longer time scales are examined either by visiting sites burned several decades earlier (e.g., [13, 48]) or using a space-for-time approach (e.g., [12]), leaving knowledge gaps in the progression of change following wildfire. A recent study by Helbig et al. [49] used satellite observations across North American boreal forests to assess long-term trends following wildfire (> 70 years) and noted summer daytime warming trends far outcompeted wintertime cooling trends. Yet ground truth observations were absent for the Canadian subarctic, and impacts to permafrost were only speculative. Few studies have continually and directly monitored ground thermal regimes for several years following wildfire in boreal permafrost settings [14], and none to the authors' knowledge have done so in peatland-dominated landscapes. In particular, an integrated perspective that combines the surface radiation balance with subsurface measurements (e.g., moisture content, temperature, and permafrost) is needed. In response, this study continuously monitored surface and subsurface conditions of a burned and unburned portion of a peat plateau for 10 years following a wildfire (2014–2024) with the objectives to (1) determine the progressive changes in the surface radiation balance following wildfire, (2) evaluate the dominant seasonal controls on the subsurface thermal regime, and (3) assess the resulting effects on subsurface processes, including thermal and moisture regimes and permafrost stability. Measurements included subcanopy meteorological variables (e.g., wind speed and net radiation and its components), snow depth and SWE, and subsurface variables including temperature, moisture content, and depth to permafrost.

## 2 | Methods

### 2.1 | Study Site

The study was conducted in the headwaters of the Scotty Creek basin (61°18′N, 121°18′W) in the southern Taiga Plains ecoregion approximately 50-km south of Fort Simpson, NWT (Figure 1a). The *ca*. 150-km$^2$ Scotty Creek basin is representative of the peatland-dominated lowlands of the southern Taiga Plains. About 60% of North America's boreal forests lie in the zones of discontinuous permafrost (50% to < 90% of the land surface contains permafrost) and sporadic permafrost (10% to < 50%) (e.g., [50–52]). The climate is continental with short dry summers and long cold winters [53]. Measurements at Fort Simpson Airport between 1991 and 2020 indicate a mean annual air temperature of −2.3°C and average annual precipitation of 370.5 mm with 33% falling as snow [54]. Snowmelt typically commences near the end of March or early April, and ground surfaces are largely snow-free by early May [55].

The landscape in the upper half of the Scotty Creek basin is relatively flat and covered by peat plateaus and thermokarst wetlands (also known as collapse scars), which are clustered into discrete plateau-wetland complexes that are separated by channel fens that convey water to the basin outlet [56, 57]. The peat plateaus are underlain by permafrost and support a forest cover dominated by stunted (< 10 m tall) black spruce (*Picea mariana*) [58]. Their ground surfaces rise 1 to 2 m above the surrounding collapse scars and fens, which, by contrast, are permafrost-free and treeless [59, 60]. In this area, permafrost is 5 to 13 m thick [61], active layer temperatures have steadily risen since the early 2000s [62], and permafrost bodies are largely isothermal at the melting point temperature [33]. Connon et al. [31] estimated that in 2015, approximately 48% of the area is underlain by a suprapermafrost talik that separates the active layer from the underlying permafrost.

On June 18, 2014, a wildfire burned a 1.5-ha portion of a 2-ha peat plateau on the southeast edge of Goose Lake (Figure 1b). The fire was extinguished by a fire crew using fire retardant within 24 h of its initiation and was classified as low severity [63] given relatively light scorching of the ground surface [40]. The burned area sustained 100% tree mortality and removed all understory foliage, including substantial loss of lichens (*Cladonia* spp.). By the end of August 2014, Labrador tea (*Rhododendron groenlandicum*) had begun to recolonize from surviving rhizomes, and by the 2021 growing season, black spruce saplings were observed in some areas of the burn site (Figure S1). The unburned portion of the peat plateau has an overstory dominated by black spruce, while the understory consists mostly of Labrador tea, bog cranberry (*Vaccinium oxycoccos*), and some dwarf birch (*Betula glandulosa*). The ground cover is dominated by *Sphagnum* moss and lichen, which form hummocky microtopography.

Study measurements were made on both the burned ("Burn") and unburned ("Unburn") portions of the peat plateau impacted by the 2014 wildfire (Figure 1b). The Unburn was used as the control site assuming that it represents the preburn condition of the plateau. Given the proximity of the sites, it is also assumed that prior to the wildfire, they had experienced the same climatic conditions, but that since 2014, the Burn site experienced the compounding effects of wildfire.

### 2.2 | Meteorological Measurements

Data collection at the Burn and Unburn meteorological stations commenced on August 30, 2014. Both stations were instrumented to measure four-component net radiation (CNR4, Kipp and Zonen, Delft, Netherlands), air temperature (±0.1°C), and relative humidity (±1.5% at 23°C; HC-S3-XT Rotronic Instrument Corp., Bassersdorf, Switzerland), snow depth (±1 cm; SR50A acoustic sensor, temperature-corrected, Campbell Scientific Canada, Edmonton, AB), wind speed (±0.3 m/s or 1% of reading) and direction (±3°; R.M. YOUNG Model 05103, Traverse City, MI, USA), and ground temperature at 16, 32, and 46 cm below ground (±1°; Thermocouple type "T" wire, Omega Engineering, Stamford, CT, USA). Sensor heights, operating ranges, and accuracies are included in Table S1. Each station was equipped with a CR1000 data logger (Campbell Scientific, Logan UT) that took sensor

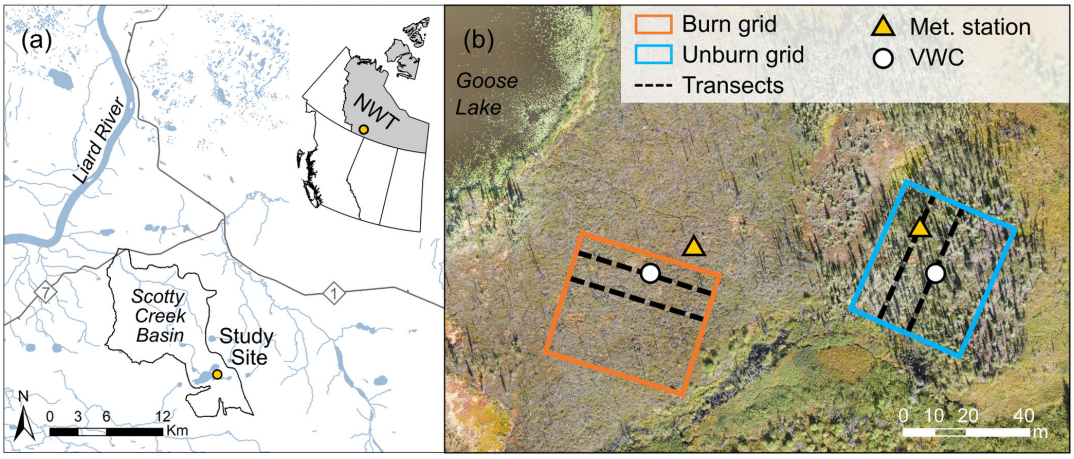


**FIGURE 1** | (a) Location of the Scotty Creek research station, ~50-km south of Fort Simpson, NWT, Canada. (b) Aerial imagery (senseFly eBee X) of the Burn and Unburn sites (August 27, 2021) with locations of grids, transects, meteorological stations, and volumetric water content (VWC) profile loggers.

measurements every 60 s and averaged and recorded data at 30-min intervals.

Data from the meteorological stations were separated into snow-free (May–August) and snow-covered (November–March) periods for each year between 2015 and 2024. Daily average values of incoming and outgoing shortwave (K↓ and K↑) and longwave (L↓ and L↑) radiation were used to compute net shortwave (K*), net longwave (L*), net radiation (Q*), and albedo (α). These radiation components along with wind speed, snow depth, and temperatures at 16-, 32-, and 64-cm depths below the ground surface were used to examine seasonal (snow-free vs. snow-covered) variation among the meteorological stations in each year. The data record was interrupted by power failures and sensor issues at the Unburn site during the snow-covered season of 2015 (149 missing days) and at the Burn site during the snow-free season of 2021 (113 missing days). Due to their duration, these gaps were left as missing data.

## 2.3 | Snowpack Measurements

Snow depth and density were measured along transects at Burn and Unburn during mid-late March or early April in 2015 [64], 2016 [40], 2022, 2023, and 2024. Snow depth was measured at intervals of five paces, and snow density at intervals between 10 and 25 paces. Snow depth was measured using a metal ruler, and density was measured using an Eastern Snow Conference 30 snow tube with a calibrated scale (underestimate error of 0.3%; [65]; GeoScientific, Vancouver, BC, Canada). A complete description of snow survey design at Scotty Creek can be found in Connon et al. [66]. The snowpack data was used to examine differences in average snow depth and snow water equivalent (SWE) between Burn and Unburn.

## 2.4 | Subsurface Measurements

### 2.4.1 | Seasonal Ground Thaw

On June 25, 2015, a grid with measurement points spaced at 5-m intervals was established at Burn (40 m × 50 m, 80 points) and at Unburn (45 m × 50 m, 90 points) (Figure 1b). In 2021, field measurements were made between June 9 and August 25 along two 50-m-long transects (20 points total) within both the Unburn and Burn grids (Figure 1b). The volumetric moisture content (VMC) integrated over the 0- to 20-cm depth range was measured at each transect point using a Hydrosense II hand-held soil moisture probe (±3%; Campbell Scientific). These measurements were postcalibrated using a calibration curve developed from unburned peat plateau samples at Scotty Creek, in which VMC was determined gravimetrically following an approach similar to Bourgeau-Chavez et al. [67]. On July 31, 2021, temperature and moisture sensors (5TM) connected to EM50 data loggers (Decagon, Pullman, WA, USA) were installed in profile to measure and record VWC at 4-, 8-, 16-, 32-, and 64-cm depths at 30-min intervals within the Burn and Unburn transects (Figure 1b).

The depth of seasonal ground thaw was measured weekly at each point on the Burn and Unburn transects between June 9 and August 25, 2021 using a 1.5-m graduated steel probe. The probe was inserted vertically into the ground at each point, and the depth to refusal was recorded. The refusal depth was used to indicate the position of the top of the frozen portion of the active layer (i.e., frost table), the top of talik when present (i.e., bottom of the active layer), or the top of permafrost (i.e., permafrost table). Where the depth to refusal increased by 20 cm or more from the previous week, it was assumed that the probe had extended into a talik below the active layer. Typical weekly increases in depth to refusal averaged $<2$ cm, while increases $\geq 20$ cm were rare, occurred only once at each affected point during the measurement period, and were therefore considered indicative of talik presence. In such a case, the depth recorded on the previous day of measurement was taken as the ALT at that transect point. It was assumed that the measurements on August 25, 2021 represented the depth to permafrost. At points where no talik was detected, the depth to permafrost was assumed to represent the bottom of the active layer.

### 2.4.2 | Permafrost Degradation

Permafrost table depth measurements at the two grids were made in late August each year from 2015 to 2024 (excluding 2020) using either a 1.5- or 2-m graduated steel rod as described above. In the case where a talik was present, late summer depth to refusal measurements could reliably indicate the top of permafrost. Where no talik was encountered, late August measurements may have underestimated the depth to permafrost and ALT, assuming thaw continued into September. For this study, however, measurements were taken at Burn and Unburn on the same day for comparison, and annual measurements were taken at similar times each year to compute trends. This is consistent with past studies at Scotty Creek [21] and within the Taiga Plains [11].

Ground surface elevation was measured at each grid point using a differential Global Positioning System (SR530 RTK, Leica Geosystems Inc., USA; ±0.02-m vertical accuracy) on August 28, 2016 and August 28, 2021. Ground surface elevation was measured and recorded at all grid points except for eight points in the Unburn grid and two points in the Burn grid, where measurements were missing due to poor GPS signal. Permafrost table elevation was derived by subtracting the manually measured permafrost depth from the ground surface elevation measured by differential GPS. The permafrost table depths for all intervening years between 2016 and 2021 were interpolated assuming a constant annual rate of permafrost thaw, as supported by hundreds of point measurements at Scotty Creek that show vertical thaw rates are linear [68]. Grid points adjacent to permafrost-free terrain wetlands (three points in the Unburn grid) were excluded to avoid the influence of lateral thaw when computing the rate of vertical thaw. In total, 78 and 79 points were used from the Burn and Unburn grids, respectively.

## 2.5 | Energy Calculations

A complete energy balance was not completed in this study, but instead, the summer-period radiation balance differences between the sites were used to indicate the relative increase in

energy available for permafrost thaw. Since permafrost thaw requires that energy input must exceed output, greater permafrost thaw at Burn would indicate a greater imbalance between energy input and output. Additionally, ground heat flux ($Q_g$) was considered in the context of Equation (1):

$$Q_g = Q_i + Q_s + Q_p \quad (1)$$

where $Q_i$ ($W\,m^{-2}$) is the energy used to melt ice in the active layer, $Q_s$ ($W\,m^{-2}$) is the sensible heat that warms the active layer or talik, and $Q_p$ ($W\,m^{-2}$) is the energy available to warm/thaw permafrost [62]. Frost probe measurements were used to calculate $Q_i$ ($W\,m^{-2}$) for each measurement interval and summed for the entire June 9 to August 25, 2021 period of measurement at the transects from the calorimetric method [69]:

$$Q_i = pfL\Delta z \quad (2)$$

where $p$ is the density of ice ($920\,kg\,m^{-3}$), $f$ is the volumetric fraction of ice, $L$ is the latent heat of fusion ($333{,}000\,J\,kg^{-1}$), and $\Delta z$ is the downward displacement (cm) of the frost table within the active layer. The peat immediately below the thawing front was assumed to be (1) saturated with ice and an irreducible liquid fraction ($f_W$) of 0.15 [70] and (2) have a porosity ($\psi$) of 0.82 [62]. For the calculation of $Q_i$, the ice fraction $f = \psi - f_W$ was therefore assumed to have a constant value of 0.67. The value of $\Delta z$, the only variable in Equation (2), was taken from the average frost table displacement measured at the Burn and Unburn transects. The $Q_i$ values computed for each measurement interval were converted to $MJ\,m^{-2}$ to estimate the cumulative $Q_i$ between 9 June to August 25, 2021.

A similar approach was used to estimate the energy consumed in lowering the permafrost table between 2016 and 2021. The value of $\Delta z$ was taken as the average permafrost table displacement measured at the Burn and Unburn grids over the 6-year time interval. This was compared against the cumulative net radiation ($\Sigma Q^*$) calculated for the snow-free season of each year from 2016 to 2021. $Q_g$ was then approximated by assuming it was 20% of $\Sigma Q^*$, as found by Hayashi et al. [62] in the same study area. For years where there was < 95% data availability for daily $Q^*$ (e.g., due to power failures), the previous years' $\Sigma Q^*$ was used as a conservative estimate.

## 2.6 | Statistical Analyses

All statistical analyses were performed using R statistical software ( [71], version 4.1.2) at the *alpha* ≤ 0.05 significance level. Prior to conducting statistical tests, all data were tested for normality using the Shapiro–Wilk normality test. Statistical differences in meteorological variables among the two sites were tested for each year using the nonparametric Kruskal–Wallis test and Dunn's post hoc test with the Bonferroni correction. The nonparametric Mann–Kendall test was used to assess whether trends exist from 2015 to 2024 in meteorological variables during the snow-cover and snow-free seasons. A breakpoint analysis [72] was used to identify temporal changes in wind speed differences between sites during the snow-free and snow-cover seasons. Differences in ground temperature, soil moisture, and frost table depth between Unburn and Burn were assessed using the nonparametric Mann–Whitney *U* test. Mean differences in ALT and talik thickness between the Burn and Unburn were evaluated using a two-sample *t*-test, given their normal distributions and insignificant variances. Statistical differences in annual permafrost depths below ground surface between Burn and Unburn were tested for each year using the nonparametric Kruskal–Wallis test and Dunn's post hoc test with the Bonferroni correction. The nonparametric Mann–Kendall test was used to assess whether trends exist from 2015 to 2024 in annual permafrost depths below ground surface at each site. Comparison of ground surface elevation, permafrost table elevation, and the amount of subsidence that occurs between 2016 and 2021 was achieved using the Mann–Whitney *U* test.

# 3 | Results

## 3.1 | Meteorology

### 3.1.1 | Surface Radiation

Neither the Burn nor the Unburn had any significant trends for the four components of radiation during the 10 years of the study when considering the complete time series (Mann–Kendall analysis). However, we observed substantial differences between Burn and Unburn during snow-free and snow-covered periods, and some of these differences tended to increase over the study (indicated by a significant trend in Dunn's Z-value) rather than decrease, as might be expected with post-fire recovery. For both the snow-covered and snow-free periods, K↓ (Figure 2a) and K↑ (Figure 2b) were significantly higher at Burn in every year (2015–2024) except in the snow-free periods of 2016 and 2021. Power failures at Burn during the snow-free period of 2021 limited the analysis to only the days where data were available at both sites, which likely led to insignificant differences during this year for most radiation components. We observed increasing differences between Burn and Unburn during the snow-covered periods for both K↓ ($p < 0.01$) and K↑ ($p < 0.01$) from 2016 to 2024. Sensor failure at Unburn precluded site comparisons of radiation components during the snow-covered period of 2015. During the snow-free period, the difference in K↓ significantly increased ($p = 0.02$), but K↑ did not ($p = 0.11$), resulting in K* at Burn becoming significantly higher than Unburn, but only after 2019 (Figures S2). During the snow-covered period, K* was only significantly higher at Burn in 2019, 2021, and 2023.

By the summer of Year 4 (2018), L↓ became significantly lower at Burn than Unburn, with significant differences occurring more frequently after Year 7 (2021) for both the snow-free and snow-covered periods (Figure 2c). L↑ was only significantly higher at Burn in the snow-free periods of 2015 and 2022 (Figure 2d). L* was significantly lower at Burn for all snow-free periods, except 2016 and 2021 (Figures S2 and S3). In the snow-covered period, L* was only lower at Burn in 2021 and 2023.

As expected, following a fire, α was significantly lower at Burn in the first year after the fire (2015) (Figure 3a). However, α was significantly higher at Burn for every snow-free season after that (except 2021), with the greatest differences observed in Years 8–10 (Figure 3b). For the snow-covered period, Burn

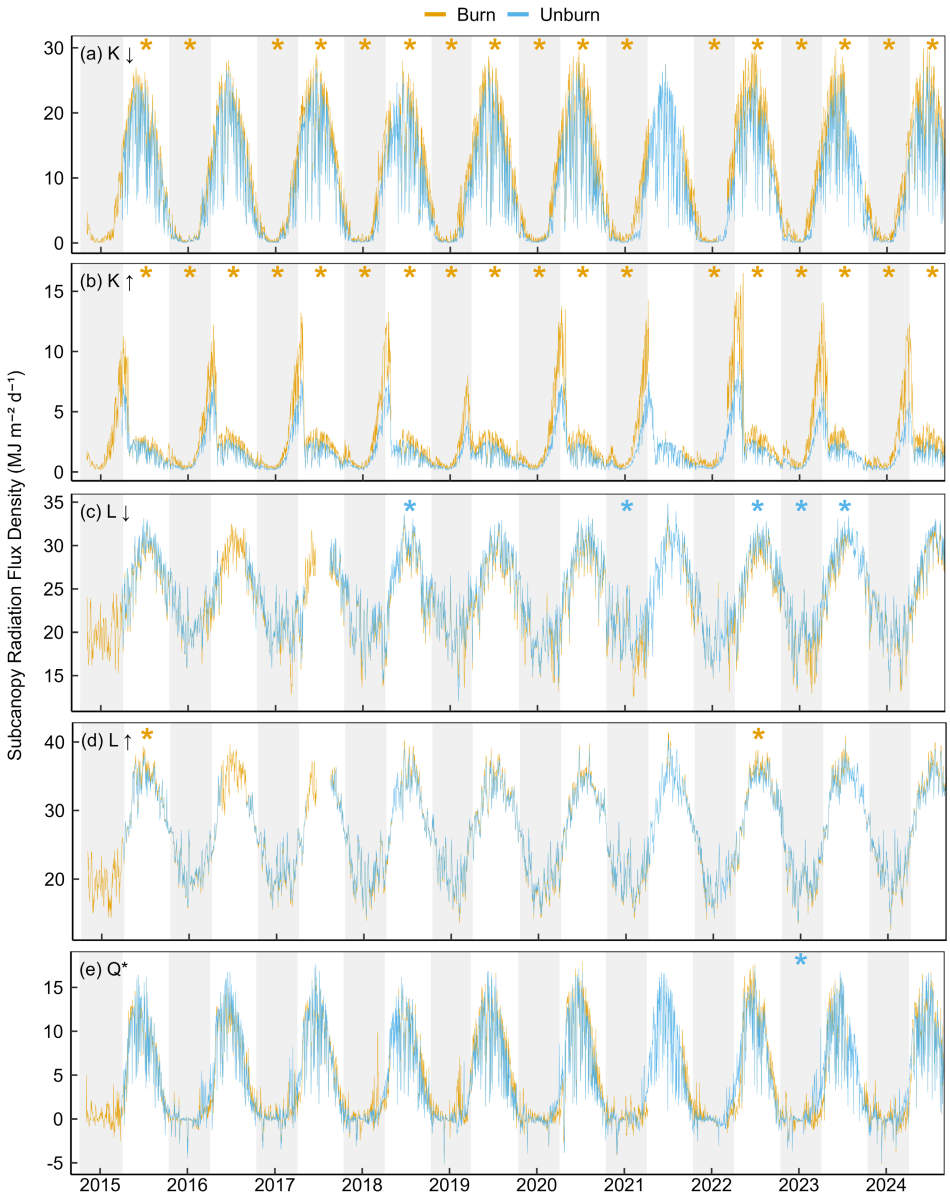


**FIGURE 2** | Measurements of (a) incoming shortwave: K↓, (b) outgoing shortwave: K↑, (c) incoming longwave: L↓, (d) outgoing longwave: L↑, and (e) net radiation: Q* measured by the Burn and Unburn stations each year. All radiation measurements are in $MJ\,m^{-2}\,d^{-1}$. Snow-cover periods are shaded in gray, and significant differences ($alpha \leq 0.05$) between sites for seasonal means are indicated with an asterisk (*), color-coded to denote the site with the greater values. Note: Data is missing from the Unburn station in 2015 and the Burn station in 2021 due to power loss.

had significantly higher α in 2016, 2017, 2020, 2023, and 2024 (Figure 3a).

Despite significant differences found in each of the four radiation components, these were balanced enough to prevent any significant differences in daily Q*, except during the snow-covered period of 2023 (Figure 2e). However, cumulative Q* (ΣQ*) at the end of each snow-free period was consistently higher at Burn than at Unburn starting in Year 3 (2017; Table 1). ΣQ* at Burn significantly increased over the study period ($p = 0.035$), but no trend was present at Unburn ($p = 0.39$). As a result, the percent difference between the sites increased over the study period, although not significant at the 0.05 level ($p = 0.068$). These trends were in the absence of any trend in the number of snow-free days, which would increase ΣQ*.

### 3.1.2 | Wind Speed and Snow Depth

Wind speeds were significantly higher at Burn throughout the entire study period (Figure 4), apart from the snow-covered period in 2015. During the snow-covered period, a break point analysis revealed that the difference in wind speed between the sites significantly increased until 2020 ($p < 0.01$); after which, there were weak and insignificant trends ($p = 0.17$; Figure S3). The same breakpoint was identified for wind speeds during the snow-free period with significant increasing trends until 2020 ($p < 0.01$) and weak insignificant trends ($p = 0.38$) from 2020 to 2024. From the Mann–Kendall trend analysis, average daily wind speeds at Burn increased significantly over the entire study period ($p < 0.01$), whereas no trend in wind speed was detected at Unburn ($p = 0.99$). Wind speeds

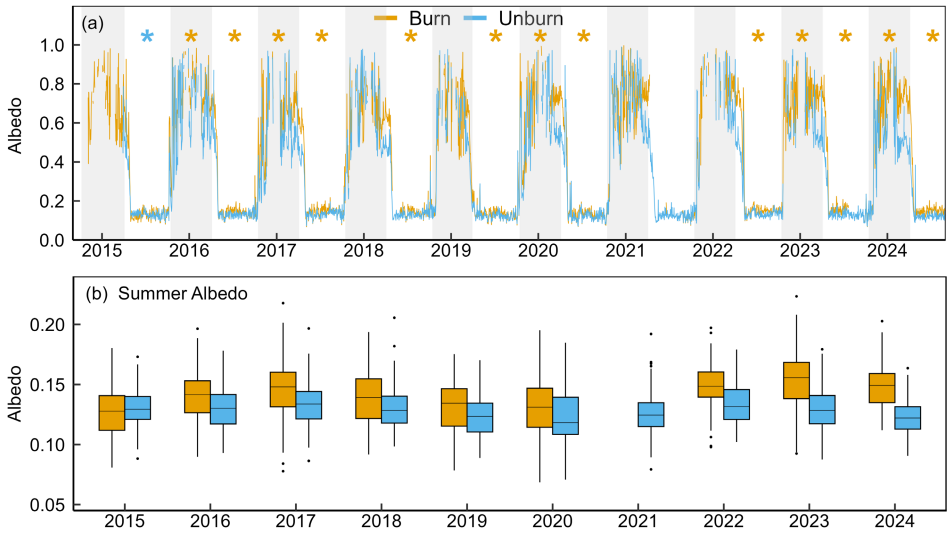


**FIGURE 3** | (a) Daily albedo (α) and (b) summer α measured by the Burn and Unburn stations. Significant differences (*alpha* ≤ 0.05) between sites for seasonal means are indicated with an asterisk (*), color-coded to denote the site with the greater values.

**TABLE 1** | Cumulative net radiation (ΣQ*) over the snow-free period for each year measured at the Burn and Unburn stations. The snow-free period was estimated from snow depth and albedo (α). Since the estimated snow-off and snow-on dates were nearly identical (±1 day) at Burn and Unburn, the same period is used for both sites. Only years with at least 95% data coverage were included.

| Year | Snow-free period | Total snow-free days | Burn ΣQ* (MJ) | Unburn ΣQ* (MJ) | Difference (MJ) | Difference (%) |
|---|---|---|---|---|---|---|
| 2015 | Apr 29–Oct 9 | 163 | 1314 | 1308 | 5.8 | 0.4 |
| 2016 | Apr 30–Oct 14 | 167 | 1368 | 1382 | −14.4 | −1.1 |
| 2017 | May 1–Oct 13 | 165 | 1401 | 1359 | 42.7 | 3.1 |
| 2019 | Mar 30–Oct 14 | 198 | 1569 | 1460 | 108.8 | 7.2 |
| 2020 | May 3–Oct 25 | 175 | 1399 | 1259 | 140.2 | 10.6 |
| 2022 | May 6–Oct 20 | 167 | 1447 | 1321 | 125.9 | 9.1 |
| 2024 | Apr 19–Sep 25 | 159 | 1476 | 1383 | 93.1 | 6.5 |

were also measured at two other stations located in a treeless bog and forested peat plateau north of Goose Lake during the same study period, but no trends were detected at these stations (Figure S4). Interestingly, the nearby forest wind speeds were similar to those at Unburn, whereas wind speeds at Burn only reached comparable magnitudes as the nearby treeless bog site after Year 6 (2020). By this time, it can be assumed that after several years of tree collapse and increasing wind speeds, few standing dead trees would remain. The loss of standing dead trees between 2016 and 2021 can be seen in drone images of the sites (Figure S1) and in photos of the Burn station from 2015 to 2024 (Figure S5).

Snow depth measured at Burn was significantly lower than Unburn in every year (Figure 5a), but end-of-season snow surveys indicated no significant difference in snow depth between the sites (Table 2). However, Unburn accumulated significantly deeper snow each year from October to January, compared to Burn (Figure 5b,c). Interestingly, snowmelt timing and peak snow depth are similar between sites (Figure 5a), which aligns with the end-of-season snow surveys. Although not significantly different (likely due to low sample size), SWE was 5%–13% higher on average at Burn in all years except 2022, which was a record high snowfall year (Table 2).

## 3.2 | Subsurface Processes

### 3.2.1 | Moisture Content and Ground Temperature

Depth-integrated VMC of the upper 20 cm was significantly lower at Burn in the first 2 years of measurement after the fire, but then increased to similar values as Unburn for the remainder of the study period (Figure 6). These results align with soil moisture profiles from August 2016 and 2021, which show drier soil in 2016 at Burn versus Unburn in the top 10 cm (Table S2). By 2021, average VMC was similar between sites near the ground surface (4-cm depth), but higher at the intermediate depths (i.e., 8, 16, and 32 cm) at Burn than Unburn. Average VMC in 2021 was similarly high for sites near the top of permafrost (64 cm), as expected. Ground temperatures at all measured depths (16, 32, and 64 cm below the ground surface) were significantly

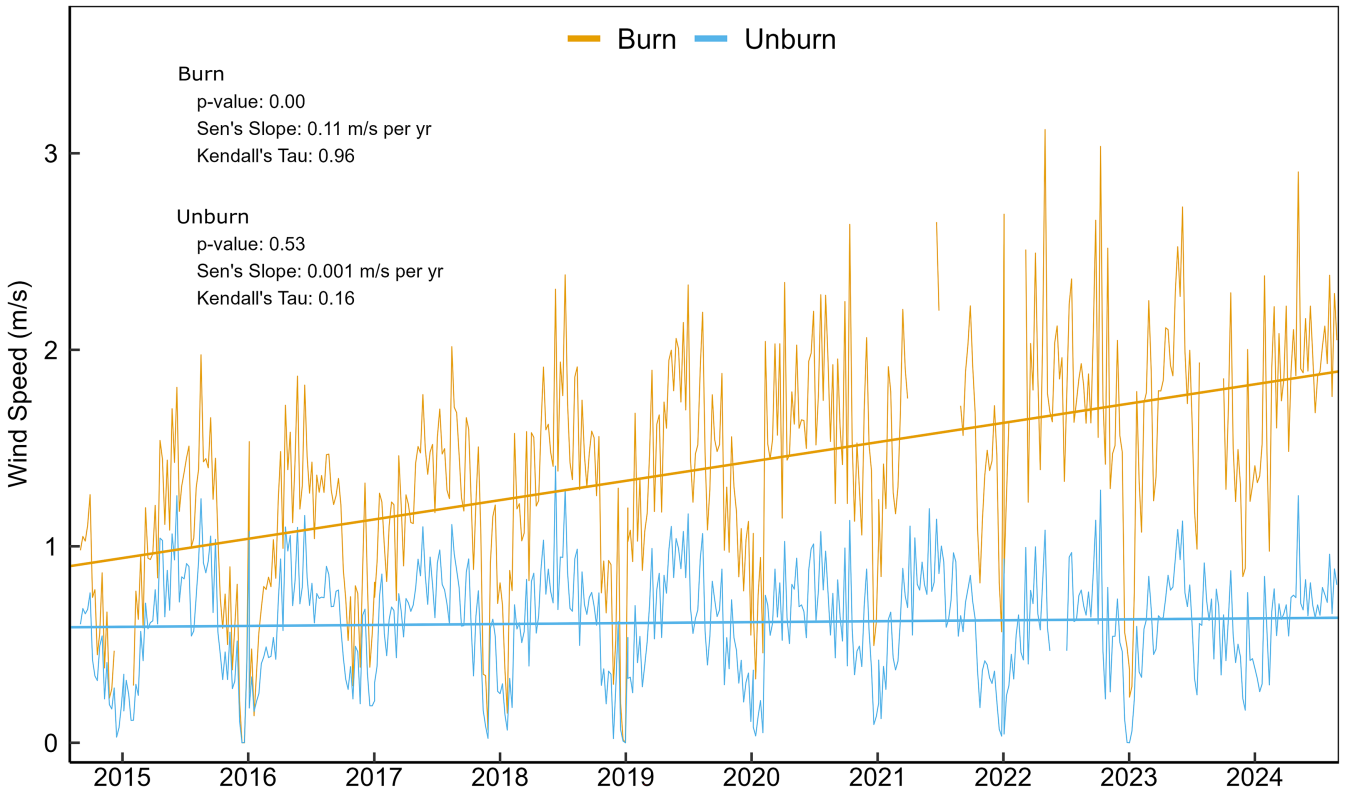


**FIGURE 4** | Average weekly wind speed measurements during the study period measured at the Burn and Unburn stations, and annual trend statistics. Thick solid lines represent the line of best fit.

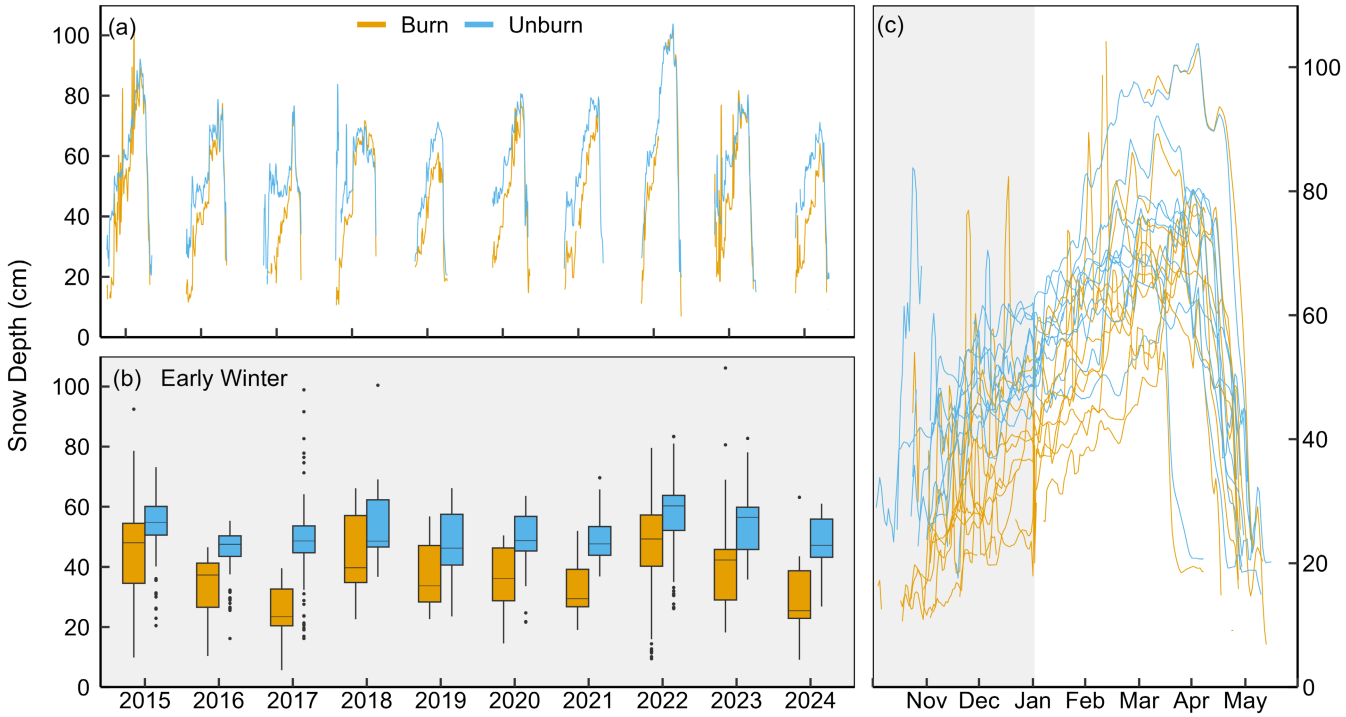


**FIGURE 5** | (a) Daily snow depth over the study period, (b) early winter (Oct–Jan) snow depth, and (c) daily snow depth (cm) for all years plotted together, measured by the Burn and Unburn stations.

warmer at Burn in every year during the snow-free periods (Figure 7a,c,e). During the snow-covered periods, Burn was significantly colder at 16 and 32 cm depths in all years during the study period (Figure 7b,d,f). At 64 cm depth, however, Burn became significantly warmer during snow-covered periods starting in Year 4 (2018) of the study.

### 3.2.2 | Active Layer Thaw

The frost probe measurements taken 7-years post-fire (2021) were significantly deeper at Burn than Unburn from June 19 until August 3, but there was no significant difference between the sites from August 10 to 25 (Figure S6). The large shift in the data distributions between July 18 and 26 at Burn, and between August 3 and 10 at Unburn, arose from numerous instances of penetration into the underlying talik. The first instance of full active layer thaw occurred nearly a month earlier at Burn (28 June) than at Unburn (26 July). Mean ALT at Burn (43.4 cm) and Unburn (47.1 cm) was not significantly different (Table 3). However, the greater ALT at Unburn resulted in a greater cumulative total latent heat used to melt ice in the active layer ($Q_i$) at that site than at Burn (Table 3). ΣQ* could not be measured in 2021 due to station power failure; however, if similar values as 2020 and 2022 are assumed, then $Q_i$ consumed 6% and 4% of the ΣQ* at Unburn and Burn, respectively, for the period June 9 to August 25.

In 2021, the permafrost table at the Burn was closest to the ground surface (61 cm) at the only measurement point, which did not have a talik below it (Figure 8a). At the remaining points, the depth to permafrost ranged between 64 and 125 cm. At Unburn, the depth to permafrost ranged from 40 to 59 cm for the points without talik, and from 105 to > 150 cm at points overlying talik (Figure 8b). The mean depth to permafrost at Burn (89.2 cm) was not significantly greater than at Unburn (80.8 cm). However, the average depth to permafrost was significantly greater for points with talik (101.4 cm) than without (48.5 cm) ($p < 0.01$). At Unburn, 47% of the measurement points had a talik, while at Burn, 95% had a talik in 2021. Although talik was not as prevalent at Unburn, the thickness of talik at that site was significantly greater than at the Burn (Table 3).

**TABLE 2** | Average (±1 SD) snowpack depth and SWE obtained from snow surveys conducted in late March—early April at Burn and Unburn. Differences presented are relative to Unburn, where a positive value indicates more snow (i.e., higher SWE at Burn).

| | Burn | | | | Unburn | | | | Difference (%) | |
|---|---|---|---|---|---|---|---|---|---|---|
| | Snow depth (cm) | *n* | SWE (mm) | *n* | Snow depth (cm) | *n* | SWE (mm) | *n* | Snow depth | SWE |
| 2015 | 82 ± 7 | 20 | 183 ± 12 | 4 | 83 ± 4 | 12 | 169 ± 27 | 3 | −1.2 | 8.5 |
| 2016 | 66 ± 5 | 69 | 141 ± 8 | 14 | 68 ± 7 | 66 | 134 ± 20 | 13 | −3.0 | 5.1 |
| 2022 | 90 ± 11 | 15 | 174 ± 39 | 8 | 85 ± 6 | 19 | 183 ± 28 | 9 | 5.7 | −5.0 |
| 2023 | 67 ± 12 | 19 | 122 ± 16 | 3 | 65 ± 8 | 17 | 107 ± 8 | 4 | 3.0 | 13.1 |
| 2024 | 50 ± 7 | 14 | 91 ± 7 | 3 | 49 ± 6 | 15 | 80 ± 16 | 3 | 2.0 | 12.9 |

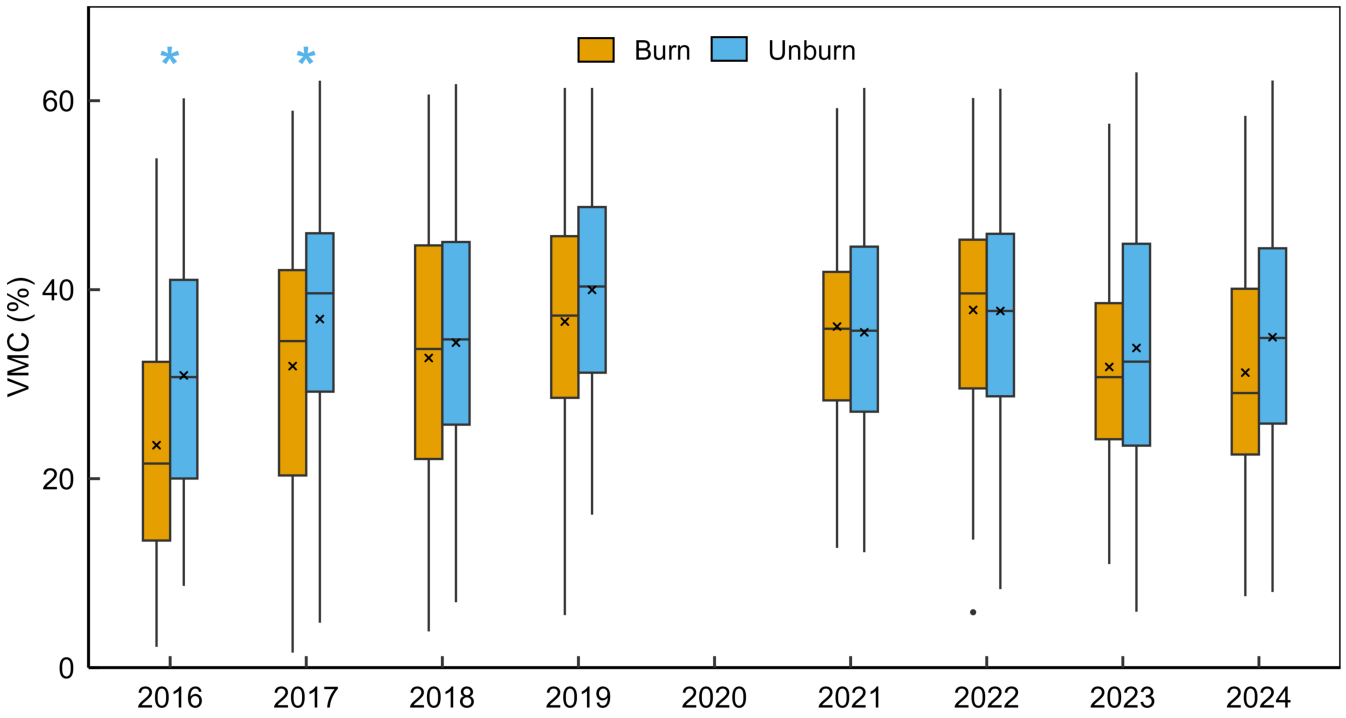


**FIGURE 6** | Depth-integrated volumetric moisture content (VMC) of the upper 20 cm at the Burn and Unburn site at grids near the end of the thaw season (late August or early September) each year from 2016 to 2024. Annual averages are indicated on the boxplots by crosses, and significant differences ($alpha \leq 0.05$) between sites are indicated with an asterisk (*), color-coded to denote the site with the greater values.

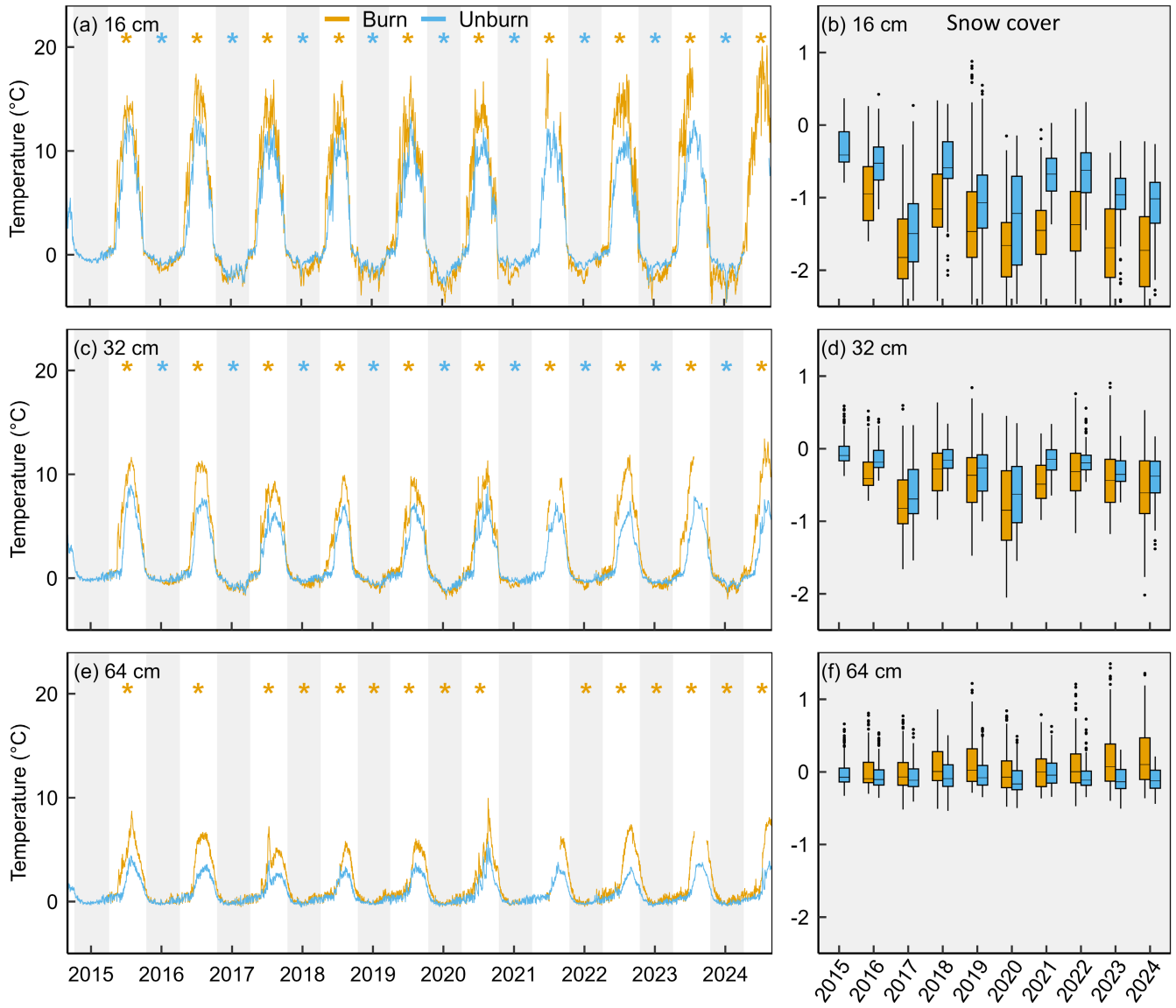


**FIGURE 7** | Ground temperatures at 16 cm (a-b), 32 cm (c-d), and 64 cm (e-f) below ground surface measured at the Burn and Unburn stations over the study period. The left column (a, c & e) presents average daily temperature, and the right column (b, d & f) displays seasonal temperatures for the snow-covered period each year. *Note:* Data from the Burn station during the 2015 snow-cover period were omitted due to lack of data owing to sensor issues. Significant differences (*alpha* ≤ 0.05) between sites for seasonal means are indicated with an asterisk (*), colour-coded to denote the site with the greater values.

**TABLE 3** | Summary of active layer thickness (ALT), talik thickness, and depth to permafrost below ground surface at the Burn and Unburn site measured between June 9 and August 25 2021. Cumulative total latent heat used to melt ice in the active layer ($Q_i$) has also been estimated for the same period. Where applicable, statistically significant differences between sites are indicated by *.

| | Burn | | | | Unburn | | | |
|---|---|---|---|---|---|---|---|---|
| | ALT (cm) | Talik thickness (cm) | Depth to permafrost (cm) | $Q_i$(MJ) | ALT (cm) | Talik thickness (cm) | Depth to permafrost (cm) | $Q_i$(MJ) |
| Average | 43.4 | 48* | 89.2 | 33.1 | 47.1 | 80.2* | 80.8 | 42.8 |
| Min | 29.5 | 25 | 61 | 13.4 | 36 | 61 | 40 | 30.8 |
| Max | 61 | 85 | 125 | 41.1 | 64 | > 113 | > 150 | 48.2 |

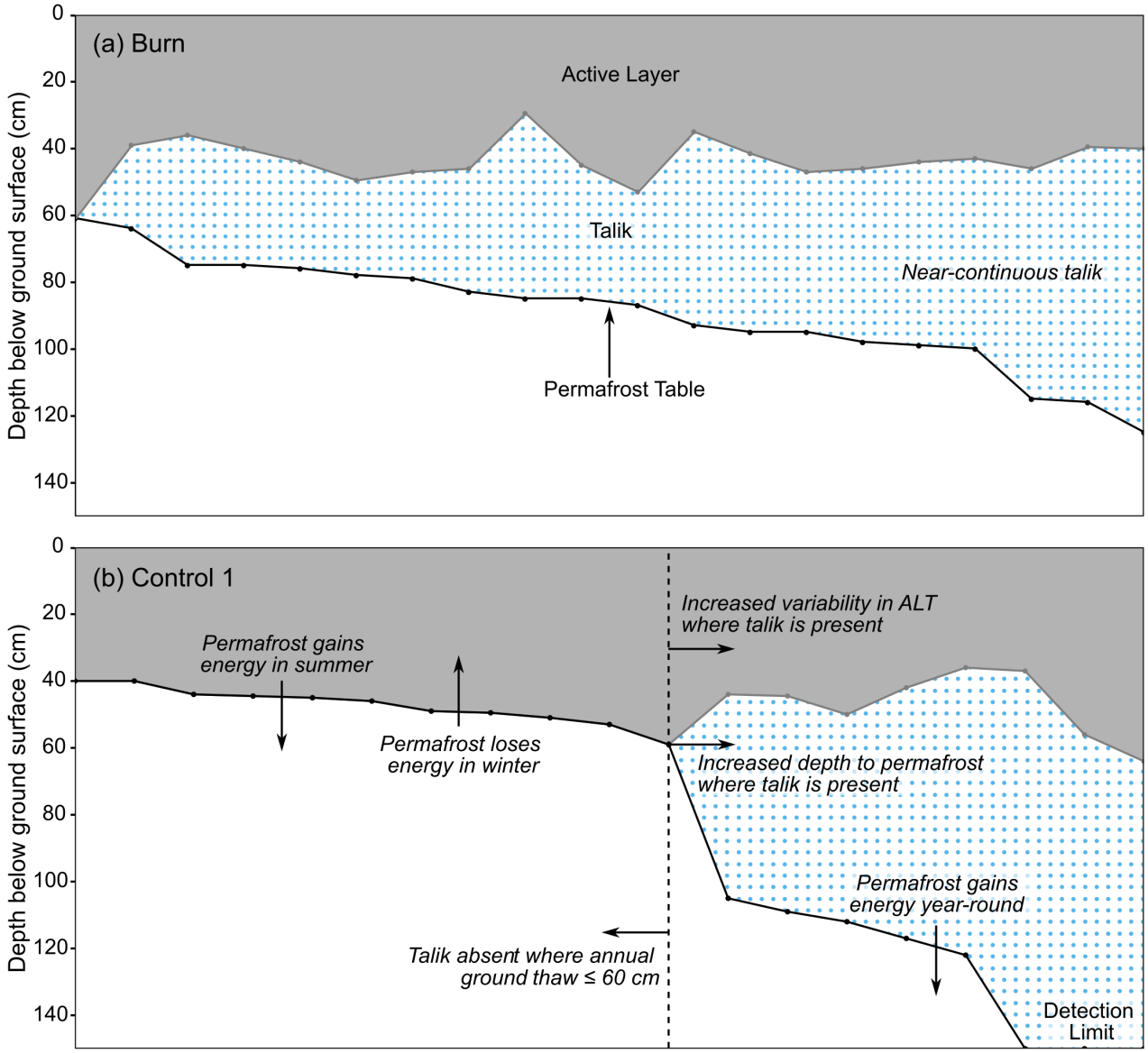


**FIGURE 8** | Active layer thickness, talik thickness, and depth to permafrost table at (a) Burn and (b) Unburn obtained from transect data over thaw season in 2021, sorted in order from shallowest to deepest.

**TABLE 4** | Average ground surface elevation (MASL), permafrost table elevation (MASL), ground/permafrost subsidence between 2016 and 2021, and depth to permafrost below ground surface at the Burn and Unburn grids in 2016 and 2021. Statistically significant differences in the amount of subsidence/permafrost table lowering between sites are indicated by an asterisk (*).

| | Burn | | | Unburn | | |
|---|---|---|---|---|---|---|
| | 2016 | 2021 | Subsidence (m) | 2016 | 2021 | Subsidence (m) |
| Ground surface avg. (MASL) | 286.40 | 286.06 | 0.34* | 285.80 | 285.48 | 0.32 |
| Permafrost table avg. (MASL) | 285.58 | 285.10 | 0.48* | 284.95 | 284.60 | 0.35 |
| Depth to refusal avg. (m) | 0.82 | 0.96 | 0.14 | 0.87 | 0.87 | 0 |

### 3.2.3 | Permafrost Thaw

Both the ground surfaces and the permafrost tables lowered significantly at the Burn and Unburn between 2016 and 2021 (Table 4). The rates of subsidence of both the ground surface and permafrost table between 2016 and 2021 were significantly higher at the Burn than Unburn (Table 4). The average annual rate of permafrost thaw over this period was 10 cm at the Burn and 6 cm at the Unburn (Figure 9). [31] suggested the threshold for talik formation at Scotty Creek was between 60 and

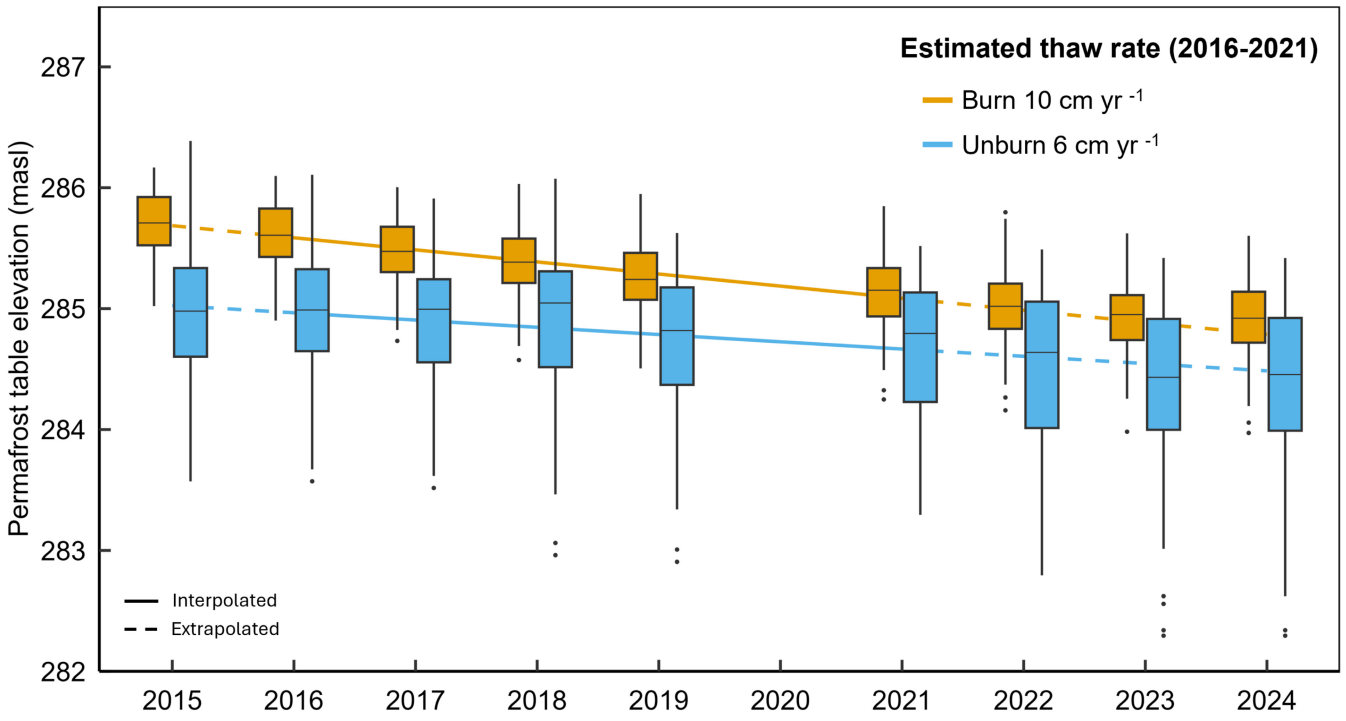


**FIGURE 9** | Permafrost table elevation (masl) measured at the Burn and Unburn sites obtained from manual measurements at the end of the annual ground thaw period (late August to early September) between 2015-024, combined with elevation measurements taken in 2016 and 2021. Estimated thaw rates are based on mean annual values. *Note:* measurements were not taken in 2020.

80 cm below ground surface based on late winter measurements (April) of the suprapermafrost layer thickness (SLT) using a frost probe and ice auger. When SLT was < 60 cm, there was complete refreeze over winter (i.e., no talik found), but for measurements > 80 cm, a talik was always present (i.e., threshold for talik formation). Here, the threshold for talik formation was determined from the depth to refusal results from the 2021 thaw season, where the maximum depth for complete winter refreeze (i.e., no talik found) was 61 cm at Burn and 64 cm at Unburn (Table 3; Figure 8). Using a conservative threshold of 70 cm below ground surface at both sites, the occurrence of talik increased by 53% at the Burn and 19% at Unburn from 2015 to 2024, where 95% of the Burn grid points were underlain by talik by Year 5 (2019; Table S3). In 2015, 48% of the grid points at the Burn were underlain by talik, whereas 58% of the grid points at Unburn were underlain by talik. By 2024, talik occurred below 100% of the points at the Burn and 77% of the points at Unburn.

## 4 | Discussion

A decade of near-continuous measurements of surface radiation, snow dynamics, and permafrost state (thermal and physical) indicated that the increased rate of permafrost thaw at Burn was driven by the gradual loss of standing dead trees, which amplified summertime energy availability at the site (ΣQ*). The reduced surface albedo due to charring of the ground was not a key driver of ground warming as it was counteracted by the rapid proliferation of Labrador tea (within 2 years) with higher-albedo foliage. The effects of wildfire on the subsurface thermal regime were delayed by 4 to 5 years due to the partial shading provided by the abundant standing dead trees and the energy consumed to thaw the active layer and form a talik. The greatest effects occurred 8 to 10 years after fire once most standing dead trees had fallen and a continuous talik (100% extent) decoupled the subsurface from atmospheric cooling in winter (Figure 10). The thinner active layer at Burn also meant more energy could be directed toward ground heating and thawing of permafrost instead of seasonal frost. Although the wildfire altered the wintertime energy balance such that Burn had colder shallow ground (16–32 cm) in winter, this effect was outcompeted by the amplified summertime energy accumulation (i.e., year-over-year increases in ΣQ*). Details of the 10-year post-wildfire progression and key controls on the surface radiation balance and subsurface thermal regime are discussed below.

### 4.1 | Progression in the Surface Energy Balance

In the year following the fire, shortwave radiation (K↓ and K↑) was greater at the Burn than the Unburn, and remained greater for all 10 years of the study (Figure 2a,b; Figure 10). This was expected, considering forest canopy shading reduces the direct K↓ reaching the ground and snow surfaces [37]. In contrast to other wildfire studies [14], reductions in α were only observed in the first year after the fire, which may have been partly due to the low-severity fire (Figure 10d). However, by Year 2, α at Burn increased above Unburned and remained higher for the remainder of the study, which coincided with the rapid regrowth of Labrador tea (*R. groenlandicum*) at the Burn. It is common for low-stature shrubs such as Labrador tea to proliferate in peatlands following fire [73], especially when shrub roots are

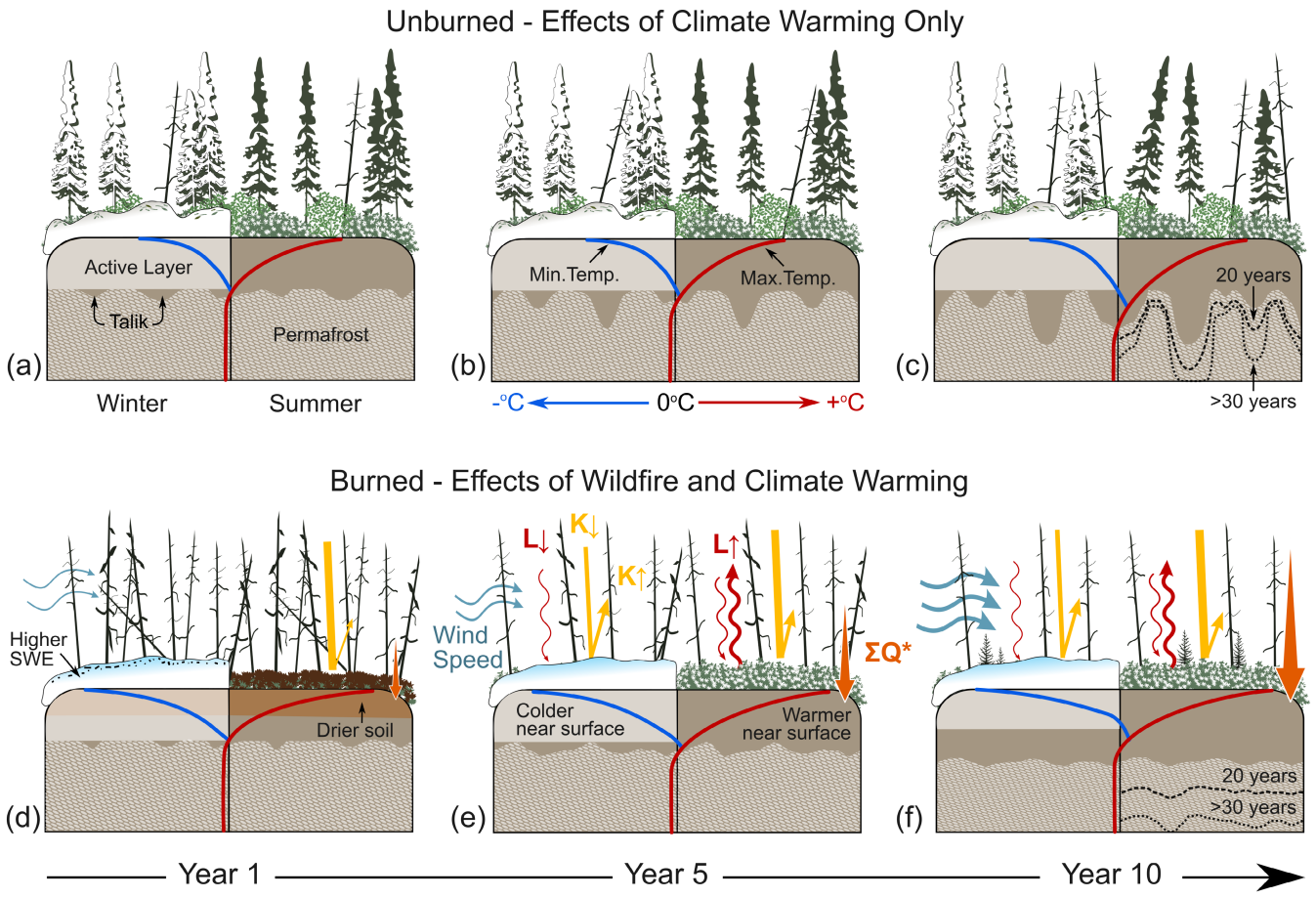


**FIGURE 10** | Conceptual model for the 10-year progression in winter (snow cover) and summer (snow free) conditions for an unburned (Top) and burned (bottom) peat plateau. The arrows shown in the lower half indicate a change in meteorological variable following fire, which includes either a change between Burn and Unburn (e.g., comparing K↓ from a to d) or over time at Burn (e.g., wind speed from d to f). The thickness of the arrows indicates the relative magnitude of change in each meteorological variable (i.e., wind, incoming shortwave [K↓], outgoing shortwave [K↑], incoming longwave [L↓], outgoing longwave [L↑], and cumulative net radiation [ΣQ*]). ***Unburned Control (top)***: (a) Year 1—suprapermafrost taliks are present due to ongoing climate warming; (b) Year 5—taliks deepen where the canopy thins and trees become waterlogged and die; (c) Year 10—taliks are further deepened and warmed until they develop into collapse scar wetlands 20–30 years into the future. ***Burned Site (bottom)***: (d) Year 1—removal of tree canopy increases wind speed, which increases SWE in winter. Scorching of the ground decreases albedo in summer and incoming solar radiation increases with a thinner canopy. Near-surface ground temperatures are colder in winter and warmer in summer compared to the unburned control; (e) Year 5—standing dead trees continue to blow down, which further increases wind speeds and lowers L↓. Albedo increases in winter due to less forest litter and increases in summer due to proliferation of Labrador Tea; (f) Year 10—Continued loss of standing dead trees further increases wind speed resulting in year-over-year increases in ΣQ* (Years 1–10). More uniform energy inputs lead to warmer ground, continuous talik development, and sustained lowering of the permafrost table and ground surface subsidence. No permafrost recovery is expected for both the Burned and Unburned sites.

undamaged and there is a post-fire increase in both available nutrients and sunlight [74]. Given the dominance of Labrador tea at the Burn and its abundant white blooms, this rapid vegetation succession explains the relatively short-lived reduction in α followed by an increase at Burn (Figure 10e). The higher α at Burn in the winter of Year 2 (Figure 3a), particularly in late winter, indicated a lack of organic litter from the canopy (Figure 10e).

In response to the absorption of radiation, the dryer ground surface of Burn in the snow-free period of Year 1 (Figure 6) enabled it to warm more readily and thereby produce a greater L↑ than at Unburn (Figure 2d), similar to the finding by Chambers et al. [39]. Although daily L↑ became similar between the sites by Year 2, the consistently lower negative values of L* at the Burn (Figure S2) indicated a greater net removal of longwave energy (Figure 10e). L↓ only became significantly lower at the Burn than Unburn in Year 4 (Figures 2c and 10), suggesting a considerable proportion of charred black spruce trunks likely remained in the first few years after the fire. L↓ decreased relative to Unburn once a higher proportion of the dead standing trees were blown down at the Burn around Years 4 and 5 (see further discussion below). During the snow-covered period, differences in longwave radiation fluxes among the sites were far less pronounced due to less effective heating of tree canopies and due to the equalizing effect of the snow cover on L↑ (Figure 2d).

It may appear that the decreases in L* and increases in K* were balanced in both snow-covered and snow-free periods, as

evidenced by no statistical difference in daily Q* between the Burn and Unburn for most years (Figure 2e). However, when Q* was summed over the entire snow-free period (ΣQ*), there was not only more cumulative energy input at the Burn, but this energy input continued to increase for the entire 10-year study period (Table 1; Figure 10f). Potential drivers and impacts of this are discussed in the proceeding sections.

### 4.2 | Effects of Standing Dead Tree Loss

Higher wind speeds at Burn than Unburn were expected due to the reduced surface roughness following forest canopy removal [46, 75]. However, the significant increasing trend in wind speed over the 10-year study period has not been reported in the literature (Figure 4). The lack of any interannual trend in wind speed at other nearby sites (Figure S5) suggests that the year-to-year increase at the Burn was driven by localized changes in the years since the fire. The increasing wind speed trend can be attributed to the gradual loss of the standing dead black spruce trunks and trees that are more prone to windthrow. As a result, aerodynamic resistance continued to decrease beyond that from the initial canopy removal until a threshold was reached in which only stable burnt trees were left, or those remaining had little effect on wind speed (Figure 10e,f). This notion was further supported by the stabilization of wind speeds around Year 6 marking this threshold was reached (Figure S3).

Burles and Boon [46] also noted that there was considerably more tree blowdown at a burn site in the second year of their 2-year study compared to the first year, and that monitoring temporal changes in forest structure following fire would help with interpreting L* and simulating Q*. Although burned forest restructuring was not monitored in detail here, the increase in deadfall was observed through drone imagery (Figure S1) and ground photos of the Burn station (Figure S5). The gradual removal of standing dead trees also explains the increase in radiative energy observed at Burn (Figure 1b). This included the increasing difference in K↓ flux between Burn and Unburn, the increasing trend in ΣQ* (Table 1), and the delayed increase in K* at the burn by Year 5 (Figure S2). Burnt standing dead trees also make an important contribution to L↓ [76], so the gradual removal of this energy source explains why L↓ becomes lower at the Burn by Year 4 for both snow-covered and snow-free periods (Figure 10e).

The gradual loss of standing dead trees may be particularly important for low-severity fires such as this one where the majority of burnt trees and trunks were left largely intact. Considering wind speeds generally stabilized by Year 6, the length of this stabilization period may be correlated with burn severity. For example, one extreme can be represented by high-severity burns, where there is immediate and complete loss of vegetation resulting in an immediate shift in the surface energy balance. The opposite extreme would be represented by this study, where the fire was low enough in severity as to only remove underbrush vegetation but high enough to lead to wholesale tree mortality. Further work on this relationship is warranted to extend findings to a wider range of burn scenarios.

### 4.3 | Competing Seasonal Controls on the Subsurface Thermal Regime

Wildfire has the potential to alter the radiation balance through a variety of wintertime and summertime processes, yet its relative importance in driving permafrost thaw was not well known. Results from this study indicate that multiple wintertime processes worked to cool shallow ground, but this was outcompeted by summertime warming and talik formation, as evidenced by greater rates of permafrost thaw (Figure 9). Previous work has attributed increases in ground temperature to thicker snowpacks following fire due to reduced canopy snow interception and sublimation (e.g., [14, 46]), but direct evidence of this is limited [9]. In contrast, this study found no statistical difference in end-of-season snow depth (Table 2) but significantly lower snow depths during early winter (October–January) at Burn (Figure 5). It was assumed that the forest density between plots was initially comparable due to the proximity of the sites, but any differences in initial forest structure would play a role in canopy capture or lack thereof. SWE was typically higher by the end of the snow-covered season at Burn (Table 2), which was likely due to a combination of reduced canopy interception [46] and snow densification by wind-compaction [40]. Both a thinner snowpack during early winter at Burn and a denser snowpack explain the lower ground temperatures observed at Burn throughout winter (Figures 7 and 10). Indeed, Jafarov et al. [16] had postulated that greater wind speeds in open-burned forests could compact the snowpack and reduce its insulating effects, but this is the first field-based evidence of this.

The lack of significant difference in end-of-winter α for the first year following fire was in contrast to findings of other studies [43, 44], which may be because the effect of ash and soot on α at the Burn was comparable to that from forest litter scattered on the snow surface at the Unburn (Figure 10). Additionally, the automatic snow depth sensors and α measurements indicated no difference in snow ablation rates in spring, although this may be due to poor spatial representativeness. After Year 2, α was higher more frequently at the Burn during winter, which could also be driven by gradual loss of standing trees and therefore less ash and litter available to cover the snow surface. The reduction in ↓L [76] and increased circulation from the loss of standing dead trees suggest radiative cooling in winter [46, 47]. When this was combined with a higher α, denser snowpack, and thinner early-winter snow depth, these wintertime processes all drove colder near-surface (16–32 cm) ground temperatures at Burn (Figure 7). Yet, summertime processes clearly outcompeted these cooling effects as evidenced by higher ΣQ* and greater rates of permafrost thaw at Burn (Figure 9). Although at different spatial and temporal scales, [49] also found summer surface warming outcompeted wintertime cooling following wildfire.

### 4.4 | Effects on Subsurface Processes

The relatively low VMC, and therefore lower volumetric heat capacity, in the first 2 years following fire (Figure 6) likely enabled the near-surface layer (0–20 cm) of the Burn to warm and cool more readily than Unburn (Figures 7 and 10). Drier surface soils are common immediately following fire [9, 40, 41] but can quickly equilibrate with understory re-growth [9] as observed

in this study with the proliferation of Labrador tea and near-surface soil moisture equilibration by Year 4 (Figure 10). Despite this, the Burn continued to have high variability in ground temperatures at 16 and 32 cm and ultimately higher rates of thaw. This may be explained by the relatively high moisture contents in the 8- to 32-cm depth range also having higher thermal conductivity, which would facilitate the conduction of energy downward. At the Unburn site, the relatively constant temperatures just below 0°C at 64 cm during winter (Figure 7) suggest a zero curtain and a cryotic talik [77]. In contrast, the ground temperatures at the Burn at 64 cm only became significantly higher than the Unburn in Year 4, with average winter temperatures above zero indicating more extensive warming and talik development.

Regardless of the site, ALT was thinner (43.87 ± 7.01 cm) at points with talik compared to points without talik (48.5 ± 6.7 cm), which aligns with findings by Connon et al. [31]. Although average ALT measured in 2021 was not significantly different between the sites ($N = 20$), the presence of a near-continuous talik at Burn would suggest a generally thinner active layer (Figure 10f). With a lower ALT on average at Burn, a lower proportion of the ground heat flux ($Q_g$) was consumed by latent heat ($Q_i$, Table 3), leaving more energy for warming the active layer and talik ($Q_s$). As a result, the first instance of complete active layer thaw occurred nearly a month earlier along the Burn frost table transects than the Unburn transects (Figure S6). The surplus of energy at the Burn (Table 1) would therefore be available to drive other subsurface processes such as talik formation and permafrost thaw. In agreement with Connon et al. [31], the depth threshold for talik formation was 60 cm. Beyond this, the ALT became both thinner and more variable, with a marked increase in talik thickness and depth to permafrost, particularly at the Unburn site (Table 3; Figure 8). The removal of the tree canopy at the Burn resulted in more uniform energy inputs in summer and winter (Figure 10), leading to a more uniform permafrost table (Figure 8) compared to the Unburn, where the spatial variation of K↓ was greater due to canopy shading effects (Figure 10a-c). This resulted in more localized (sub)surface runoff and greater maximum depths of permafrost (Table 3; [57]).

Permafrost at Scotty Creek is at its maximum temperature (i.e., ice nucleation) [68] owing to persistent climate warming over recent decades [14, 20]. As a result, all additional energy input to permafrost ($Q_p$) is available to support the phase change and permafrost thaw. It was estimated that the energy required to displace the permafrost table between 2016 and 2021 (Table 4) at the Burn exceeded that at Unburn by 27 MJ. Assuming approximately 20% of the $\sum Q^*$ was converted to $Q_g$ [62], the additional energy available to thaw permafrost at the Burn compared to Unburn between 2016 and 2021 would have been 89 MJ during the snow-free season. Therefore, the extra $\sum Q^*$ at the Burn can more than account for the extra permafrost thaw at that site relative to Unburn, even after considering $Q_i$ needed for active layer thaw. It should be noted that the thinner active layer at the Burn (requiring 9.7 MJ less to thaw) and the almost ubiquitous extent of talik would also result in greater permafrost thaw per unit energy flux into the ground, since less energy is partitioned to $Q_i$.

While Unburn exhibited talik development and permafrost thaw resulting from climate warming alone (Figures 8b and 10a-c), Burn demonstrated the combined effect of climate warming and fire. Within 5 years of the fire, approximately 95% of Burn was underlain by talik, despite Unburn starting with a higher talik extent (Table S3). These findings align with inferences made by Gibson et al. [12] who suggested talik extent increased in the first 15–20 years after historical fires followed by permafrost recovery to pre-fire conditions. Given the current and future climate are warmer than the conditions examined by Gibson et al. [12] (1960s–2010s), it is highly unlikely the taliks will close and the permafrost under the Burn site will recover. At Scotty Creek, taliks are not only perennially thawed but also perennially saturated. The greater energy requirements needed to refreeze saturated peat, combined with heat transfer from the talik to permafrost over winter (Figure 8), virtually decouples permafrost from the atmosphere and prevents it from cooling over winter. For this reason, the formation of talik is a "tipping point" that either initiates or greatly accelerates permafrost thaw [33]. The persistence of permafrost 10-year post-fire also aligns with Shur and Jorgenson [10], who suggested that for climate-driven, ecosystem-protected permafrost, wildfire disturbance leads to irreversible permafrost thaw, but it may take decades to centuries before it is completely lost.

### 4.5 | Implications

This study identified increased summertime energy as the main driver of post-fire permafrost thaw, which suggests that as summers grow longer under climate warming [78], the effects of wildfire will have greater impacts on permafrost in the coming decades. Findings also showed that enhanced wintertime cooling occurred due to post-fire changes to snowpack dynamics. However, if winters become shorter in the future, any cooling that occurs will likely diminish and rates of thaw will further increase. Such permafrost thaw in boreal peatland complexes has cascading effects on landcover (e.g., [3]), hydrology (e.g., [79]), water quality (e.g., [80]), greenhouse gas emissions (e.g., [81]), and biogeochemical cycling (e.g., [82]). For example, as permafrost thaws, forested peat plateaus that once impeded subsurface flow are converted to permafrost-free bogs and fens [57], which become increasingly connected to the basin drainage network [79]. The increased groundwater flow and associated nutrients, combined with expanded anoxic wetland extent, support more suitable environments for both contaminant (e.g., methylmercury) and greenhouse gas production (e.g., methane) ([11, 81]). Additionally, the conversion of peat plateaus to bogs and fens affects critical caribou habitat and traditional land use [83].

Not only do the findings from this study indicate that coupled thermo-hydro-biogeochemical processes may occur at faster rates following wildfire, but the spatial patterns of thaw will change considerably due to a more homogenous lowering of the frost table. Rather than thermokarst occurring in isolated patches, like in unburned areas, gradual subsidence across an entire burned area will likely result in wholesale conversion to thermokarst wetlands. Yet, the formation of a continuous and hydrologically connected talik may provide better subsurface drainage across the site, which helps reduce the permafrost thaw feedback that occurs when subsurface water pools above permafrost [33]. Future work is still needed to fully disentangle the trajectory of coupled hydrological, biogeochemical, and

atmospheric processes, but data and results from this study will aid in process-based modeling efforts.

## 5 | Conclusions

This study monitored surface and subsurface processes of a burned and unburned portion of a forested peat plateau for 10 years (2014–2024) following a low-severity wildfire in a boreal peatland complex near the southern limit of permafrost in western Canada. Specific objectives of the study were to understand the post-fire succession of the surface balance and the associated effects on the subsurface thermal regime, and assess the relative importance of winter versus summertime processes in driving permafrost thaw.

Results demonstrated that the gradual loss of standing dead trees following the low-severity fire amplified summertime energy inputs (ΣQ*) providing more available energy for ground heating and permafrost thaw (4 cm year$^{-1}$ higher on average). The reduced surface albedo due to charring of the ground was not a key driver of ground heating as it was counteracted by the rapid proliferation of Labrador tea (within 2 years) with higher-albedo foliage. Similarly, alterations to the snowpack (e.g., densified snowpack, lower early winter snow accumulation, and higher snow albedo) led to cooler shallow ground (16–32 cm) during winter, yet not enough to offset increased energy availability in summer. The effects of fire on the subsurface thermal regime were delayed by 4–5 years due to partial shading of the standing dead trees and energy consumed by thawing seasonal frost and talik formation. Since taliks resulted in thinner active layers, the formation of a near-continuous talik (95% extent) at Burn by Year 5 meant more energy was available for thawing permafrost instead of the active layer. As a result, the full effects of wildfire on permafrost were only observed toward the end of the study period (Years 8–10), once most standing dead trees were gone and talik extent was highest.

Given current climate trajectories, longer, warmer summers and shorter winters likely mean wildfire will have even greater effects on permafrost in the future, and it is unlikely permafrost under either study site will recover. The decade-long monitoring in this study was the first to capture both the gradual progression of the surface radiation balance and identify the key drivers of permafrost thaw following wildfire. With the 64, 312-ha fire that swept through the Scotty Creek basin in 2022, there is an opportunity for future work to build on these findings to explore the effects of higher severity fire on the landscape trajectory of the Taiga Plains and associated impacts to northern boreal peatlands.


### Acknowledgments

We gratefully acknowledge Łíídlıı̨ Kų́ę́ First Nation, on whose traditional lands this research was conducted. This research was funded by ArcticNet. D.O. received support for the research from the National Science and Engineering Research Council Discovery grant (RGPIN-2016-04688). O.S. acknowledges support through the Canada Research Chair (CRC-2018-279 00259), NSERC Discovery Grants (DGPIN-280 2018-05743) and FQRNT Projet de Recherche en Équipe programs (RQ000082), and the Global Water Futures project.


### Conflicts of Interest

The authors declare no conflicts of interest.

### Data Availability Statement

The data that support the findings of this study are available from the corresponding author upon reasonable request.

### References


1. T. A. Moon, M. L. Druckenmiller, and R. L. Thoman, *NOAA Arctic Report Card 2024: Executive Summary* (United States Government, 2024), https://doi.org/10.25923/B7C7-6431.

2. S. L. Smith, H. B. O'Neill, K. Isaksen, J. Noetzli, and V. E. Romanovsky, "The Changing Thermal State of Permafrost," *Nature Reviews Earth and Environment* 3 (2022): 10–23, https://doi.org/10.1038/s43017-021-00240-1.

3. O. Carpino, K. Haynes, R. Connon, J. Craig, É. Devoie, and W. Quinton, "Long-Term Climate-Influenced Land Cover Change in Discontinuous Permafrost Peatland Complexes," *Hydrology and Earth System Sciences* 25 (2021): 3301–3317, https://doi.org/10.5194/hess-25-3301-2021.

4. J. M. Young, A. Alvarez, J. van der Sluijs, et al., "Recent Intensification (2004–2020) of Permafrost Mass-Wasting in the Central Mackenzie Valley Foothills Is a Legacy of Past Forest Fire Disturbances," *Geophysical Research Letters* 49 (2022): e2022GL100559, https://doi.org/10.1029/2022GL100559.

5. W. Li, D. Yan, B. Weng, and L. Zhu, "Research Progress on Hydrological Effects of Permafrost Degradation in the Northern Hemisphere," *Geoderma* 438 (2023): 116629, https://doi.org/10.1016/j.geoderma.2023.116629.

6. J.-M. St. Jacques and D. J. Sauchyn, "Increasing Winter Baseflow and Mean Annual Streamflow From Possible Permafrost Thawing in the Northwest Territories, Canada," *Geophysical Research Letters* 36 (2009): 1–6, https://doi.org/10.1029/2008GL035822.

7. K. Burd, S. E. Tank, N. Dion, et al., "Seasonal Shifts in Export of DOC and Nutrients From Burned and Unburned Peatland-Rich Catchments, Northwest Territories, Canada," *Hydrology and Earth System Sciences* 22 (2018): 4455–4472, https://doi.org/10.5194/hess-22-4455-2018.

8. M. Helbig, C. Pappas, and O. Sonnentag, "Permafrost Thaw and Wildfire: Equally Important Drivers of Boreal Tree Cover Changes in the Taiga Plains, Canada," *Geophysical Research Letters* 43 (2016a): 1598–1606, https://doi.org/10.1002/2015GL067193.

9. J. E. Holloway, A. G. Lewkowicz, T. A. Douglas, et al., "Impact of Wildfire on Permafrost Landscapes: A Review of Recent Advances and Future Prospects," *Permafrost and Periglacial Processes* 31 (2020): 371–382, https://doi.org/10.1002/ppp.2048.

10. Y. L. Shur and M. T. Jorgenson, "Patterns of Permafrost Formation and Degradation in Relation to Climate and Ecosystems," *Permafrost and Periglacial Processes* 18 (2007): 7–19, https://doi.org/10.1002/ppp.582.

11. S. N. Wright, L. M. Thompson, D. Olefeldt, et al., "Thaw-Induced Impacts on Land and Water in Discontinuous Permafrost: A Review of the Taiga Plains and Taiga Shield, Northwestern Canada," *Earth-Science Reviews* 232 (2022): 104104, https://doi.org/10.1016/j.earscirev.2022.104104.

12. C. Gibson, L. E. Chasmer, D. K. Thompson, W. L. Quinton, M. D. Flannigan, and D. Olefeldt, "Wildfire as a Major Driver of Recent Permafrost Thaw in Boreal Peatlands," *Nature Communications* 9 (2018): 3041, https://doi.org/10.1038/s41467-018-05457-1.

13. C. R. Burn, "The Response (1958-1997) of Permafrost and Near-Surface Ground Temperatures to Forest Fire, Takhini River Valley, Southern Yukon Territory," *Canadian Journal of Earth Sciences* 35 (1998): 184–199, https://doi.org/10.1139/e97-105.

14. S. L. Smith, D. W. Riseborough, and P. P. Bonnaventure, "Eighteen Year Record of Forest Fire Effects on Ground Thermal Regimes and Permafrost in the Central Mackenzie Valley, NWT, Canada," *Permafrost and Periglacial Processes* 26 (2015): 289–303, https://doi.org/10.1002/ppp.1849.

15. C. C. Hanes, X. Wang, P. Jain, M.-A. Parisien, J. M. Little, and M. D. Flannigan, "Fire-Regime Changes in Canada Over the Last Half Century," *Canadian Journal of Forest Research* 49 (2019): 256–269, https://doi.org/10.1139/cjfr-2018-0293.

16. E. E. Jafarov, V. E. Romanovsky, H. Genet, A. D. McGuire, and S. S. Marchenko, "The Effects of Fire on the Thermal Stability of Permafrost in Lowland and Upland Black Spruce Forests of Interior Alaska in a Changing Climate," *Environmental Research Letters* 8 (2013): 035030, https://doi.org/10.1088/1748-9326/8/3/035030.

17. P. Jain, Q. E. Barber, S. W. Taylor, et al., "Drivers and Impacts of the Record-Breaking 2023 Wildfire Season in Canada," *Nature Communications* 15 (2024): 6764, https://doi.org/10.1038/s41467-024-51154-7.

18. B. M. Wotton, M. D. Flannigan, and G. A. Marshall, "Potential Climate Change Impacts on Fire Intensity and Key Wildfire Suppression Thresholds in Canada," *Environmental Research Letters* 12 (2017): 095003, https://doi.org/10.1088/1748-9326/aa7e6e.

19. Y. Zhang, S. A. Wolfe, P. D. Morse, I. Olthof, and R. H. Fraser, "Spatiotemporal Impacts of Wildfire and Climate Warming on Permafrost Across a Subarctic Region, Canada," *Journal of Geophysical Research: Earth Surface* 120 (2015): 2338–2356, https://doi.org/10.1002/2015JF003679.

20. B. K. Biskaborn, S. L. Smith, J. Noetzli, et al., "Permafrost Is Warming at a Global Scale," *Nature Communications* 10 (2019): 264, https://doi.org/10.1038/s41467-018-08240-4.

21. W. Quinton, A. Berg, M. Braverman, et al., "A Synthesis of Three Decades of Hydrological Research at Scotty Creek, NWT, Canada," *Hydrology and Earth System Sciences* 23 (2019): 2015–2039, https://doi.org/10.5194/hess-23-2015-2019.

22. V. Romanovsky, M. Burgess, S. Smith, K. Yoshikawa, and J. Brown, "Permafrost Temperature Records: Indicators of Climate Change," *Eos, Transactions American Geophysical Union* 83 (2002): 589–594, https://doi.org/10.1029/2002EO000402.

23. D. W. Beilman, D. H. Vitt, and L. A. Halsey, "Localized Permafrost Peatlands in Western Canada: Definition, Distributions, and Degradation," *Arctic, Antarctic, and Alpine Research* 33 (2001): 70–77, https://doi.org/10.1080/15230430.2001.12003406.

24. R. J. E. Brown, *Permafrost Investigations on the MacKenzie Highway in Alberta and MacKenzie District* (National Research Council of Canada. Division of Building Research, 1964), https://doi.org/10.4224/20358861.

25. Y. T. J. Kwong and T. Y. Gan, "Northward Migration of Permafrost Along the Mackenzie Highway and Climatic Warming," *Climatic Change* 26 (1994): 399–419, https://doi.org/10.1007/BF01094404.

26. S. D. Robinson and T. R. Moore, "The Influence of Permafrost and Fire Upon Carbon Accumulation in High Boreal Peatlands, Northwest Territories, Canada," *Arctic, Antarctic, and Alpine Research* 32 (2000): 155–166, https://doi.org/10.2307/1552447.

27. D. W. Beilman and S. D. Robinson, "Peatland Permafrost Thaw and Landform Type Along a Climatic Gradient," in *Proceedings of the Eighth International Conference on Permafrost*, vol. 1 (International Permafrost Association, 2003), 6.

28. P. Camill and J. S. Clark, "Climate Change Disequilibrium of Boreal Permafrost Peatlands Caused by Local Processes," *American Naturalist* 151 (1998): 207–222, https://doi.org/10.1086/286112.

29. S. C. Zoltai, "Cyclic Development of Permafrost in the Peatlands of Northwestern Alberta, Canada," *Arctic and Alpine Research* 25 (1993): 240–246, https://doi.org/10.2307/1551820.

30. J. L. Baltzer, T. Veness, L. E. Chasmer, A. E. Sniderhan, and W. L. Quinton, "Forests on Thawing Permafrost: Fragmentation, Edge Effects, and Net Forest Loss," *Global Change Biology* 20 (2014): 824–834, https://doi.org/10.1111/gcb.12349.

31. R. Connon, É. Devoie, M. Hayashi, T. Veness, and W. Quinton, "The Influence of Shallow Taliks on Permafrost Thaw and Active Layer Dynamics in Subarctic Canada," *Journal of Geophysical Research: Earth Surface* 123 (2018): 281–297, https://doi.org/10.1002/2017JF004469.

32. H. B. O'Neill, P. Roy-Leveillee, L. Lebedeva, and F. Ling, "Recent Advances (2010–2019) in the Study of Taliks," *Permafrost and Periglacial Processes* 31 (2020): 346–357, https://doi.org/10.1002/ppp.2050.

33. É. G. Devoie, J. R. Craig, R. F. Connon, and W. L. Quinton, "Taliks: A Tipping Point in Discontinuous Permafrost Degradation in Peatlands," *Water Resources Research* 55 (2019): 9838–9857, https://doi.org/10.1029/2018WR024488.

34. P. Camill, "Peat Accumulation and Succession Following Permafrost Thaw in the Boreal Peatlands of Manitoba, Canada," *Écoscience* 6 (1999): 592–602, https://doi.org/10.1080/11956860.1999.11682561.

35. A. B. K. Sannel and P. Kuhry, "Warming-Induced Destabilization of Peat Plateau/Thermokarst Lake Complexes," *Journal of Geophysical Research: Biogeosciences* 116 (2011): 1–16, https://doi.org/10.1029/2010JG001635.

36. D. M. Rey, M. A. Walvoord, B. J. Minsley, B. A. Ebel, C. I. Voss, and K. Singha, "Wildfire-Initiated Talik Development Exceeds Current Thaw Projections: Observations and Models From Alaska's Continuous Permafrost Zone," *Geophysical Research Letters* 47 (2020): e2020GL087565, https://doi.org/10.1029/2020GL087565.

37. L. Chasmer, W. Quinton, C. Hopkinson, R. Petrone, and P. Whittington, "Vegetation Canopy and Radiation Controls on Permafrost Plateau Evolution Within the Discontinuous Permafrost Zone, Northwest Territories, Canada," *Permafrost and Periglacial Processes* 22 (2011): 199–213, https://doi.org/10.1002/ppp.724.

38. N. Wright, M. Hayashi, and W. L. Quinton, "Spatial and Temporal Variations in Active Layer Thawing and Their Implication on Runoff Generation in Peat-Covered Permafrost Terrain," *Water Resources Research* 45 (2009): 1–13, https://doi.org/10.1029/2008WR006880.

39. S. D. Chambers, J. Beringer, J. T. Randerson, and F. S. Chapin, III, "Fire Effects on Net Radiation and Energy Partitioning: Contrasting Responses of Tundra and Boreal Forest Ecosystems," *Journal of Geophysical Research: Atmospheres* 110 (2005): 1–9, https://doi.org/10.1029/2004JD005299.

40. C. Ackley, S. E. Tank, K. M. Haynes, F. Rezanezhad, C. McCarter, and W. L. Quinton, "Coupled Hydrological and Geochemical Impacts of Wildfire in Peatland-Dominated Regions of Discontinuous Permafrost," *Science of the Total Environment* 782 (2021): 146841, https://doi.org/10.1016/j.scitotenv.2021.146841.

41. N. Kettridge, R. E. Humphrey, J. E. Smith, et al., "Burned and Unburned Peat Water Repellency: Implications for Peatland Evaporation Following Wildfire," *Journal of Hydrology* 513 (2014): 335–341, https://doi.org/10.1016/j.jhydrol.2014.03.019.

42. G. Jungqvist, S. K. Oni, C. Teutschbein, and M. N. Futter, "Effect of Climate Change on Soil Temperature in Swedish Boreal Forests," *PLoS ONE* 9 (2014): e93957, https://doi.org/10.1371/journal.pone.0093957.

43. K. E. Gleason, A. W. Nolin, and T. R. Roth, "Charred Forests Increase Snowmelt: Effects of Burned Woody Debris and Incoming Solar Radiation on Snow Ablation," *Geophysical Research Letters* 40 (2013): 4654–4661, https://doi.org/10.1002/grl.50896.

44. T. M. Uecker, S. D. Kaspari, K. N. Musselman, and S. M. Skiles, "The Post-Wildfire Impact of Burn Severity and Age on Black Carbon Snow Deposition and Implications for Snow Water Resources, Cascade Range, Washington," *Journal of Hydrometeorology* 21 (2020): 1777–1792, https://doi.org/10.1175/JHM-D-20-0010.1.

45. M. Woo and M. A. Giesbrecht, "Simulation of Snowmelt in a Subarctic Spruce Woodland: 1. Tree Model," *Water Resources Research* 36 (2000): 2275–2285, https://doi.org/10.1029/2000WR900094.

46. K. Burles and S. Boon, "Snowmelt Energy Balance in a Burned Forest Plot, Crowsnest Pass, Alberta, Canada," *Hydrological Processes* 25 (2011): 3012–3029, https://doi.org/10.1002/hyp.8067.

47. S. M. Stuenzi, J. Boike, W. Cable, et al., "Variability of the Surface Energy Balance in Permafrost-Underlain Boreal Forest," *Biogeosciences* 18 (2021): 343–365, https://doi.org/10.5194/bg-18-343-2021.

48. J. E. Holloway and A. G. Lewkowicz, "Half a Century of Discontinuous Permafrost Persistence and Degradation in Western Canada," *Permafrost and Periglacial Processes* 31 (2020): 85–96, https://doi.org/10.1002/ppp.2017.

49. M. Helbig, L. Daw, H. Iwata, L. Rudaitis, M. Ueyama, and T. Živković, "Boreal Forest Fire Causes Daytime Surface Warming During Summer to Exceed Surface Cooling During Winter in North America," *AGU Advances* 5 (2024): e2024AV001327, https://doi.org/10.1029/2024AV001327.

50. S. Gruber, "Derivation and Analysis of a High-Resolution Estimate of Global Permafrost Zonation," *Cryosphere* 6 (2012): 221–233, https://doi.org/10.5194/tc-6-221-2012.

51. J. Obu, S. Westermann, A. Bartsch, et al., "Northern Hemisphere Permafrost Map Based on TTOP Modelling for 2000–2016 at 1 km$^2$ Scale," *Earth-Science Reviews* 193 (2019): 299–316, https://doi.org/10.1016/j.earscirev.2019.04.023.

52. M. Helbig, K. Wischnewski, N. Kljun, et al., "Regional Atmospheric Cooling and Wetting Effect of Permafrost Thaw-Induced Boreal Forest Loss," *Global Change Biology* 22 (2016b): 4048–4066, https://doi.org/10.1111/gcb.13348.

53. MSC—Meteorological Service of Canada, *National Climate Data Archive of Canada* (Environment Canada, 2017).

54. ECCC, "Canadian Climate Normals 1981-2010 Station Data. [WWW Document]," (2021), accessed November 3, 2022, https://climate.weather.gc.ca/climate_normals/results_1981_2010_e.html?stnID=4268&autofwd=1.

55. L. Hamlin, A. Pietroniro, T. Prowse, R. Soulis, and N. Kouwen, "Application of Indexed Snowmelt Algorithms in a Northern Wetland Regime," *Hydrological Processes* 12 (1998): 1641–1657, https://doi.org/10.1002/(SICI)1099-1085(199808/09)12:10/11<1641::AID-HYP686>3.0.CO;2-W.

56. M. Hayashi, W. L. Quinton, A. Pietroniro, and J. J. Gibson, "Hydrologic Functions of Wetlands in a Discontinuous Permafrost Basin Indicated by Isotopic and Chemical Signatures," *Journal of Hydrology* 296 (2004): 81–97, https://doi.org/10.1016/j.jhydrol.2004.03.020.

57. W. L. Quinton, M. Hayashi, and L. E. Chasmer, "Peatland Hydrology of Discontinuous Permafrost in the Northwest Territories: Overview and Synthesis," *Canadian Water Resources Journal* 34 (2009): 311–328, https://doi.org/10.4296/cwrj3404311.

58. M.-È. Garon-Labrecque, É. Léveillé-Bourret, K. Higgins, and O. Sonnentag, "Additions to the Boreal Flora of the Northwest Territories With a Preliminary Vascular Flora of Scotty Creek," *Canadian Field-Naturalist* 129 (2015): 349–367, https://doi.org/10.22621/cfn.v129i4.1757.

59. C. Tarnocai, I. M. Kettles, and B. Lacelle, *Peatlands of Canada* (Geological Survey of Canada, 2011).

60. S. C. Zoltai and C. Tarnocai, "Perennially Frozen Peatlands in the Western Arctic and Subarctic of Canada," *Canadian Journal of Earth Sciences* 12 (1974): 28–43, https://doi.org/10.1139/e75-004.

61. A. F. McClymont, M. Hayashi, L. R. Bentley, and B. S. Christensen, "Geophysical Imaging and Thermal Modeling of Subsurface Morphology and Thaw Evolution of Discontinuous Permafrost," *Journal of Geophysical Research: Earth Surface* 118 (2013): 1826–1837, https://doi.org/10.1002/jgrf.20114.

62. M. Hayashi, N. Goeller, W. L. Quinton, and N. Wright, "A Simple Heat-Conduction Method for Simulating the Frost-Table Depth in Hydrological Models," *Hydrological Processes* 21 (2007): 2610–2622, https://doi.org/10.1002/hyp.6792.

63. J. E. Keeley, "Fire Intensity, Fire Severity and Burn Severity: A Brief Review and Suggested Usage," *International Journal of Wildland Fire* 18 (2009): 116–126, https://doi.org/10.1071/WF07049.

64. E. Mathieu, "The Effects of Fire on Snow Accumulation, Snowmelt and Ground Thaw on a Peat Plateau in Subarctic Canada" (MSc Thesis, Wilfrid Laurier University, Waterloo, Ontario, 2018), https://scholars.wlu.ca/etd/2048.

65. P. E. Farnes, N. R. Peterson, B. E. Goodison, and R. P. Richards, "Metrication of Manual Snow Sampling Equipment by Western Snow Conference Metrication Committee. In Proceedings of the 50th Annual Western Snow Conference," in *50th Annual Western Snow Conference* (Western Snow Conference, 1982), 120–132.

66. R. F. Connon, L. Chasmer, E. Haughton, et al., "The Implications of Permafrost Thaw and Land Cover Change on Snow Water Equivalent Accumulation, Melt and Runoff in Discontinuous Permafrost Peatlands," *Hydrological Processes* 35, no. 9 (2021): e14363, https://doi.org/10.1002/hyp.14363.

67. L. L. Bourgeau-Chavez, G. C. Garwood, K. Riordan, B. W. Koziol, and J. Slawski, "Development of Calibration Algorithms for Selected Water Content Reflectometry Probes for Burned and Non-Burned Organic Soils of Alaska," *International Journal of Wildland Fire* 19 (2010): 961–975, https://doi.org/10.1071/WF07175.

68. É. G. Devoie, J. R. Craig, M. Dominico, et al., "Mechanisms of Discontinuous Permafrost Thaw in Peatlands," *Journal of Geophysical Research: Earth Surface* 126 (2021): e2021JF006204, https://doi.org/10.1029/2021JF006204.

69. M. Woo and Z. Xia, "Effects of Hydrology on the Thermal Conditions of the Active Layer: Paper Presented at the 10th Northern Res. Basin Symposium (Svalbard, Norway—28 Aug./3 Sept. 1994)," *Hydrology Research* 27 (1996): 129–142, https://doi.org/10.2166/nh.1996.0024.

70. W. L. Quinton, T. Shirazi, S. K. Carey, and J. W. Pomeroy, "Soil Water Storage and Active-Layer Development in a Sub-Alpine Tundra Hillslope, Southern Yukon Territory, Canada," *Permafrost and Periglacial Processes* 16 (2005): 369–382, https://doi.org/10.1002/ppp.543.

71. R Development Core Team, *R: A Language and Environment for Statistical Computing* (R Foundation for Statistical Computing, 2021).

72. A. Zeileis, F. Leisch, K. Hornik, and C. Kleiber, "Strucchange: An R Package for Testing for Structural Change in Linear Regression Models," *Journal of Statistical Software* 7, no. 2 (2002): 1–38.

73. E. A. Jones, L. E. Chasmer, K. J. Devito, and C. D. Hopkinson, "Shortening Fire Return Interval Predisposes West-Central Canadian Boreal Peatlands to More Rapid Vegetation Growth and Transition to Forest Cover," *Global Change Biology* 30 (2024): e17185, https://doi.org/10.1111/gcb.17185.

74. M. Guêné-Nanchen, M.-C. LeBlanc, and L. Rochefort, "Post-Fire Peatland Vegetation Recovery: A Case Study in Open Rich Fens of the Canadian Boreal Forest," *Botany* 100 (2022): 435–447, https://doi.org/10.1139/cjb-2021-0194.

75. S. L. Dingman, *Physical Hydrology: Third Edition* (Waveland Press, 2015).

76. J. W. Pomeroy, D. Marks, T. Link, et al., "The Impact of Coniferous Forest Temperature on Incoming Longwave Radiation to Melting Snow," *Hydrological Processes* 23 (2009): 2513–2525, https://doi.org/10.1002/hyp.7325.

77. É. Devoie, R. F. Connon, R. Beddoe, J. Goordial, W. L. Quinton, and J. R. Craig, "Disconnected Active Layers and Unfrozen Permafrost: A Discussion of Permafrost-Related Terms and Definitions," *Science of the Total Environment* 912 (2024): 169017, https://doi.org/10.1016/j.scitotenv.2023.169017.

78. IPCC, *IPCC Special Report on the Ocean and Cryosphere in a Changing Climate*, ed. H.-O. Pörtner, D. C. Roberts, V. Masson-Delmotte, et al. (Cambridge University Press, 2019), https://doi.org/10.1017/9781009157964.

79. R. F. Connon, W. L. Quinton, J. R. Craig, J. Hanisch, and O. Sonnentag, "The Hydrology of Interconnected Bog Complexes in Discontinuous Permafrost Terrains," *Hydrological Processes* 29, no. 18 (2015): 3831–3847, https://doi.org/10.1002/hyp.10604.

80. L. M. Thompson, M. Low, R. Shewan, et al., "Concentrations and Yields of Mercury, Methylmercury, and Dissolved Organic Carbon From Contrasting Catchments in the Discontinuous Permafrost Region, Western Canada," *Water Resources Research* 59, no. 11 (2023): e2023WR034848, https://doi.org/10.1029/2023wr034848.

81. J. Kirkwood, H. Adam, P. Roy-Léveillée, et al., "Soil Microbial Community Response to Permafrost Degradation in Palsa Fields of the Hudson Bay Lowlands: Implications for Greenhouse Gas Production in a Warming Climate," *Global Biogeochemical Cycles* 35, no. 6 (2021): e2021GB006954, https://doi.org/10.1029/2021gb006954.

82. J. B. Korosi, J. McDonald, K. A. Coleman, et al., "Long-Term Changes in Organic Matter and Mercury Transport to Lakes in the Sporadic Discontinuous Permafrost Zone Related to Peat Subsidence," *Limnology and Oceanography* 60, no. 5 (2015): 1550–1561, https://doi.org/10.1002/lno.10116.

83. F. Calmels, C. Laurent, R. Brown, F. Pivot, and M. Ireland, "How Permafrost Thaw May Impact Food Security of Jean Marie River First Nation, NWT," in *Proceedings of the 68th Canadian Geotechnical Conference and 7th Canadian Permafrost Conference* (International Permafrost Association, 2015).

## Supporting Information

Additional supporting information can be found online in the Supporting Information section. **Table S1:** Height, operating range, and accuracy of sensors instrumented at each of the three micrometeorological stations. **Figure S1:** Vegetation recovery demonstrated through aerial imagery (eBee X) between (a) August 2016 and (b) August 2021 and photos of ground surface vegetation at the Burn site in (c) August 2014 (photo credit: David Olefeldt) and (d) July 2021. **Figure S2:** (a) Net shortwave, K* and (b) net longwave radiation, L* at the Burn and Unburn. **Figure S3:** Z-value from Kruskal–Wallis pairwise comparison of wind speed at the Burn and Unburn sites for (a) snow-covered and (b) snow-free periods. All scores were significant ($p < 0.05$), and positive indicating wind speed was greater at the Burn than Unburn site. The linear increase in the z-value indicates the sites became increasingly different until 2021–2022. **Figure S4:** Weekly wind speeds at (a) a nearby bog station (2 m above the ground surface) and (b) forested peat plateau station (1.5 m above the ground surface). No significant trends were detected for either site. **Figure S5:** Photos of the burn meteorological station from 2015 to 2024. The image from 2015 illustrates the abundant standing burnt trees remaining following the fire and the lightly scorched ground. By 2016, the dead trees began to lean, and Labrador tea dominated the subcanopy vegetation. Considerable toppling of dead trees can be observed by 2021. Further dead deadfall in 2022 reveals Goose Lake on the horizon with limited standing dead trees remaining by 2024. **Table S2:** Mean volumetric moisture content (VWC) with depth below ground surface at Burn and Unburn for the month of August in 2016 compared to 2021. The difference is relative to Unburn, where a negative value indicates VWC is lower at Burn than Unburn. **Table S3:** Percent of grid point underlain by talik assuming a 70-cm depth to permafrost threshold. **Figure S6:** Depth to frost probe refusal relative to the ground surface (GS) over the 2021 thaw season at the Burn and Unburn site. Range of depth to which the active layer extends as observed by Connon et al. [31] shown in gray. Significant differences (alpha $\leq 0.05$) between sites are indicated with an asterisk (*), color-coded to denote the site with the greater values.